

# Discrete Adjoint for Accurate Numerical Optimization with Application to Quantum Control

N. Anders Petersson<sup>a,\*</sup>, Fortino M. Garcia<sup>b</sup>, Austin E. Copeland<sup>c</sup>,  
Ylva L. Rydin<sup>d</sup>, Jonathan L. DuBois<sup>e</sup>

<sup>a</sup>Center for Applied Scientific Computing, LLNL, Livermore, CA 94550, USA.

<sup>b</sup>Department of Applied Mathematics, CU, Boulder, CO 80309, USA

<sup>c</sup>Department of Mathematics, SMU, Dallas, TX 75205, USA

<sup>d</sup>Department of Information Technology, UU, 751 05 Uppsala, SWEDEN

<sup>e</sup>Quantum Coherent Device Physics Group, LLNL, Livermore, CA 94550, USA

---

## Abstract

This paper considers the optimal control problem for realizing logical gates in a closed quantum system. The quantum state is governed by Schrödinger's equation, which we formulate as a time-dependent Hamiltonian system in terms of the real and imaginary parts of the state vector. The system is discretized with the Störmer-Verlet scheme, which is a symplectic partitioned Runge-Kutta method. Our main theoretical contribution is the derivation of a compatible time-discretization of the adjoint state equation, such that the gradient of the discrete objective function can be calculated exactly, at a computational cost of solving two Schrödinger systems, independently of the number of parameters in the control functions.

A parameterization of the control functions based on B-splines with built-in carrier waves is also introduced. The carrier waves are used to specify the frequency spectra of the control functions, while the B-spline functions specify their envelope and phase. This approach allows the number of control parameters to be independent of, and significantly smaller than, the number of time steps for integrating Schrödinger's equation.

We consider Hamiltonians that model the dynamics of a superconducting multi-level qudit and present numerical examples of how the proposed technique can be combined with the interior point L-BFGS algorithm from the IPOPT package for realizing quantum gates. In a set of test cases, the proposed algorithm is shown to compare favorably with QuTiP/pulse\_optim and Grape-Tensorflow.

*Keywords:* Optimal control, Partitioned Runge-Kutta method, Discrete adjoint, Quantum computing

---

\*Corresponding author

*Email addresses:* [petersson1@llnl.gov](mailto:petersson1@llnl.gov) (N. Anders Petersson),  
[fortino.garcia@colorado.edu](mailto:fortino.garcia@colorado.edu) (Fortino M. Garcia), [acopeland@mail.smu.edu](mailto:acopeland@mail.smu.edu) (Austin E. Copeland),  
[ylva.rydin@it.uu.se](mailto:ylva.rydin@it.uu.se) (Ylva L. Rydin), [dubois9@llnl.gov](mailto:dubois9@llnl.gov) (Jonathan L. DuBois)

---

## 1. Introduction

A key challenge for realizing the potential of quantum computing lies in determining the most efficient and accurate route to controlling the quantum states in a quantum device. This challenge stems from the fact that current quantum computing systems, unlike classical computers, do not have a fixed set of logical gates predetermined in hardware. Instead, the execution of a quantum algorithm is carried out by first devising a set of classical control functions that are then applied to the quantum computing hardware to guide the quantum states through a series of quantum logical operations [16]. Reducing the time required for a quantum gate to be realized is critical for near-term quantum computing because it enables the computation to finish before the quantum state collapses to a classical state, rendering the results meaningless. To mitigate this problem, quantum optimal control techniques have been developed to produce customized control pulses that minimize the execution time for complicated gates that directly map onto a physical system [20].

Optimizing the control functions for realizing quantum gates is an optimal control problem where the objective function measures the infidelity of the gate transformation, constrained by Schrödinger's equation governing the evolution of the quantum states. For superconducting circuits it is also important to suppress leakage into highly energetic states [13], leading to an optimal control problem in Mayer-Lagrange form. Our approach builds upon the works of Hager [9], Sanz-Serna [19] and Ober-Blöbaum [18]. Hager [9] first showed how the Hamiltonian structure in an optimization problem can be utilized to calculate the gradient of the objective function. Hager considered the case in which the state equation is discretized by one Runge-Kutta scheme, with the adjoint state equation discretized by another Runge-Kutta scheme. It was found that the discrete gradient can be calculated exactly if the pair of Runge-Kutta methods satisfy the requirements of a symplectic partitioned Runge-Kutta method. Further details and generalizations are described in the review paper by Sanz-Serna [19]. Ober-Blöbaum [18] extended Hager's approach to the case where the state equation itself is a Hamiltonian system that is discretized by a partitioned Runge-Kutta scheme. For autonomous state equations, it was shown that the compatible discretization of the adjoint state equation is another partitioned Runge-Kutta scheme.

In the quantum optimal control problem, the Schrödinger (state) equation is a time-dependent Hamiltonian system. To ensure long-time numerical accuracy it is appropriate to discretize it using a symplectic time-integration method [10]. For this purpose we use the Störmer-Verlet method, which can be written as a partitioned Runge-Kutta scheme, based on the trapezoidal and implicit midpoint rules. Our main theoretical contribution is the generalization of Ober-Blöbaum's [18] work to the case of a time-dependent Hamiltonian system. We show that the compatible method for the adjoint state equation resembles a partitioned Runge-Kutta scheme, except that the time-dependent matrices must be

evaluated at modified time levels.

Logical gates in a closed quantum system can be viewed as linear reversible mappings,  $|\psi''\rangle = V_g|\psi'\rangle$ , from an initial state  $|\psi'\rangle$  to a final state  $|\psi''\rangle$ , where the reversibility implies that the mapping  $V_g$  must be unitary,  $V_g^\dagger V_g = I$ . To introduce the quantum control problem, we start by discussing the case where the unitary transformation is defined in the entire  $N$ -dimensional state space, such that it can be represented by a unitary matrix  $V_g \in \mathbb{C}^{N \times N}$ ; a more general case is described in Section 2.

In the following, we will replace the ket-notation [16] of the state vector  $|\psi\rangle = \psi^{(0)}|0\rangle + \psi^{(1)}|1\rangle + \dots + \psi^{(N-1)}|N-1\rangle$  by the vector notation  $\boldsymbol{\psi} = \psi^{(0)}\mathbf{e}_0 + \psi^{(1)}\mathbf{e}_1 + \dots + \psi^{(N-1)}\mathbf{e}_{N-1}$ , which is more common in the computational mathematics literature<sup>1</sup>. The elements in the state vector are complex probability amplitudes and the squared magnitude of the amplitudes sum to unity, i.e.,  $\|\boldsymbol{\psi}\|_2^2 = 1$ .

To account for all admissible initial data in the Hilbert space  $\mathbb{C}^N$ , we consider the evolutions from the canonical basis vectors  $\mathbf{e}_j$ , for  $j = 0, 1, \dots, N-1$ . The time-dependent control functions are expanded in terms of a finite number of basis functions, such that the control functions are determined by the finite-dimensional parameter vector  $\boldsymbol{\alpha} \in \mathbb{R}^D$ . This leads to Schrödinger's equation in matrix form for the  $N \times N$  complex-valued solution operator matrix  $U(t, \boldsymbol{\alpha})$ :

$$\frac{dU}{dt} + iH(t, \boldsymbol{\alpha})U = 0, \quad 0 \leq t \leq T, \quad U(0, \boldsymbol{\alpha}) = I_N, \quad H^\dagger = H. \quad (1)$$

Here,  $I_N$  is the  $N \times N$  identity matrix and  $H(t, \boldsymbol{\alpha})$  is the Hamiltonian matrix, in which the time-dependence is parameterized by  $\boldsymbol{\alpha}$ . As a result, the solution operator matrix depends implicitly on  $\boldsymbol{\alpha}$  through Schrödinger's equation. Due to linearity, the solution for general initial conditions satisfies  $\boldsymbol{\psi}(t, \boldsymbol{\alpha}) = U(t, \boldsymbol{\alpha})\boldsymbol{\psi}(0, \boldsymbol{\alpha})$ .

The goal of the quantum control problem is to determine the parameter vector  $\boldsymbol{\alpha}$  such that the time-dependence in the Hamiltonian matrix leads to a solution of Schrödinger's equation that minimizes the difference between the target gate matrix  $V_g$  and  $U(T, \boldsymbol{\alpha})$ . Here, we measure the difference by the commonly used target gate infidelity [11, 13, 14, 15, 20],

$$\mathcal{J}_0(U_T(\boldsymbol{\alpha})) = 1 - \frac{1}{N^2} \left| \text{Tr} \left( U_T^\dagger(\boldsymbol{\alpha}) V_g \right) \right|^2, \quad U_T(\boldsymbol{\alpha}) := U(T, \boldsymbol{\alpha}). \quad (2)$$

Because  $U_T$  and  $V_g$  are unitary,  $|\text{Tr}(U_T^\dagger V_g)| \leq N$  and  $\mathcal{J}_0 \geq 0$ . Note that the target gate infidelity is sensitive to relative phase differences between the columns of  $U_T$  and  $V_g$ , but is invariant to global phase differences between  $U_T$  and  $V_g$ .

The quantum control problem is a constrained optimization problem where, in the basic setting, the gate infidelity (2) is minimized under the constraints that the solution operator matrix satisfies Schrödinger's equation (1) and the

---

<sup>1</sup>Here,  $\mathbf{e}_j$  represents the  $j$ th canonical basis vector, in which the  $j$ th element is one and all other elements are zero.

amplitudes of the control functions (determined by the parameter vector  $\boldsymbol{\alpha}$ ) do not exceed prescribed limits. For a discussion of the solvability of the quantum control problem, see for example Borzi et al. [3].

While not a restriction of our approach, we exemplify our technique on Hamiltonians that model the dynamics of a superconducting qudit (a qubit with more than two energy levels). We represent the state vector in the energy basis in which the system Hamiltonian matrix is diagonal. In the laboratory frame of reference, the Hamiltonian matrix is modeled by

$$H_{lab}(t, \boldsymbol{\alpha}) = \omega_a a^\dagger a - \frac{\xi_a}{2} a^\dagger a^\dagger a a + f(t, \boldsymbol{\alpha})(a + a^\dagger). \quad (3)$$

Here,  $a$  and  $a^\dagger$  are the lowering and raising matrices (see Appendix A),  $\omega_a > 0$  is the fundamental resonance frequency,  $\xi_a > 0$  is the self-Kerr coefficient and  $f(t, \boldsymbol{\alpha})$  is a real-valued control function that depends on the parameter vector  $\boldsymbol{\alpha}$ .

To slow down the time scales in the state vector, the problem is transformed to a rotating frame of reference (see Appendix A) in which the Hamiltonian matrix satisfies

$$H(t, \boldsymbol{\alpha}) = -\frac{\xi_a}{2} a^\dagger a^\dagger a a + p(t, \boldsymbol{\alpha})(a + a^\dagger) + iq(t, \boldsymbol{\alpha})(a - a^\dagger), \quad (4)$$

where  $p(t, \boldsymbol{\alpha})$  and  $q(t, \boldsymbol{\alpha})$  are the real-valued control functions in the rotating frame of reference. The control functions in the two frames are related by

$$f(t) = 2p(t) \cos(\omega_a t) - 2q(t) \sin(\omega_a t). \quad (5)$$

Several numerical methods for the quantum control problem are based on the GRAPE algorithm [12]. In this case, Schrödinger's equation is discretized in time using the second order accurate Magnus scheme [10], in which the Hamiltonian matrix is evaluated at the midpoint of each time step. A stair-step approximation of the control functions is imposed such that each control function is constant within each time step. Thus, the time step determines both the numerical accuracy of the dynamics of the quantum state *and* the number of control parameters. With  $Q$  control functions,  $M$  time steps of size  $h$ , the control functions are thus described by  $M$  times  $Q$  parameters  $\alpha_{j,k}$ . The propagator in the Magnus method during the  $j^{th}$  time step is of the form  $\exp(-ih(H_0 + \sum_k \alpha_{k,j} H_k))$ . In general, the matrices  $H_0$  and  $H_k$  do not commute, leading to an integral expression for the derivative of the propagator with respect to the parameters, which is needed for computing the gradient of the objective function. In the original GRAPE method, this integral expression is approximated by the first term in its Taylor series expansion, leading to an approximate gradient that is polluted by an  $\mathcal{O}(h^2)$  error. As the gradient becomes smaller during the optimization, the approximation error will eventually dominate the numerical gradient, which may hamper the convergence of the optimization algorithm. A more accurate way of numerically evaluating the

derivative of the time-step propagator can be obtained by retaining more terms in the Taylor series expansion, or by using a matrix commutator expansion [5]. More recently, the GRAPE algorithm has been generalized to optimize objective functions that include a combination of the target gate infidelity, integrals penalizing occupation of “forbidden states” (see Section 2) and terms for imposing smoothness and amplitude constraints on the control functions. Here, automatic differentiation is used for computing the gradient of the objective function [13]. However, the number of control parameters is still proportional to the number of time steps, which may become very large when the duration of the gate is long, or the quantum state is highly oscillatory.

As an alternative to calculating the gradient of the objective function by solving an adjoint equation backwards in time, the gradient can be calculated by differentiating Schrödinger’s equation with respect to each parameter in the control function, leading to a differential equation for each component of the gradient of the state vector. This approach, implemented in the GOAT algorithm [15], allows the gradient of the objective function to be calculated exactly, but requires  $(D+1)$  Schrödinger systems to be solved when the control functions depend on  $D$  parameters. This makes the method computationally expensive when the number of parameters is large.

Using the stair-stepped approximation of the control functions often leads to a large number of control parameters, which may hamper the convergence of the GRAPE algorithm. The total number of parameters can be reduced by instead expanding the control functions in terms of basis functions. By using the chain rule, the gradient from the GRAPE algorithm can then be used to calculate the gradient with respect to the coefficients in the basis function expansion. This approach is implemented in the GRAFS algorithm [14], where the control functions are expanded in terms of Slepian sequences.

Gradient-free optimization methods can also be applied to quantum optimal control problems. These methods do not rely on the gradient to be evaluated and are therefore significantly easier to implement. However, the convergence of these methods is usually much slower than for gradient-based techniques, unless the number of control parameters is very small. One example of a gradient-free methods for quantum optimal control is the CRAB algorithm [4].

Many parameterizations of quantum control functions have been proposed in the literature, for example cubic splines [7], Gaussian pulse cascades [6], Fourier expansions [22] and Slepian sequences [14]. This paper presents a different approach, based on parameterizing the control functions by B-spline basis functions with carrier waves, see Figure 1. Our approach relies on the observation that transitions between the energy levels in a quantum system are triggered by resonance, at frequencies which often can be determined by inspection of the system Hamiltonian. The carrier waves are used to specify the frequency spectra of the control functions, while the B-spline functions specify their envelope and phase. We find that this approach allows the number of control parameters to be independent of, and significantly smaller than, the number of time steps for integrating Schrödinger’s equation.

The remainder of the paper is organized as follows. In Section 2, we gen-

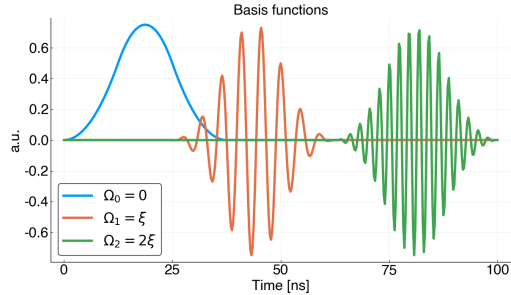


Figure 1: An example of three quadratic B-spline basis functions with carrier wave frequencies  $(0, \xi, 2\xi)$ .

eralize the optimization problem to the case of target gates that are defined in a subspace of the entire state space. In Section 3, we first introduce the real-valued formulation of Schrödinger’s equation, followed by a presentation of the symplectic Störmer-Verlet time-stepping method, written as a partitioned Runge-Kutta scheme. To achieve an exact gradient of the discrete objective function, in Section 4 we derive the discrete adjoint time integration method. This method resembles a partitioned Runge-Kutta scheme, except that the time-dependent matrices are evaluated at modified time-levels. The solution of the discrete adjoint equation is used to efficiently calculate all components of the gradient of the discrete objective function. The parameterization of the control functions using B-splines with carrier waves is presented in Section 5. Section 6 presents a numerical example of how the proposed technique can be combined with the interior point L-BFGS algorithm [17] from the IPOPT package [21] to realize multi-level qudit gates. Important properties of the optima are exposed by analyzing the eigenvalues of the Hessian. The proposed algorithm has been implemented in the JuQBox package, written in the Julia [2] programming language. In Section 7, we compare its performance to two variants of the GRAPE algorithm. Concluding remarks are given in Section 8.

## 2. Generalized gates

In quantum computing applications it is common to define gate transformations in a subspace of the entire (possibly infinite dimensional) state space, in which the evolution of higher energy states is not relevant for the gate transformation, but if left uncontrolled, may lead to leakage of probability. In the following, let the subspace of interest contain  $E > 0$  “essential” states and let  $G = N - E \geq 0$  denote the number of “guard” states. The guard states that correspond to the highest energy levels in the model are often called “forbidden” states [13].

In the case of one qudit oscillator, we can always order the elements in the state vector such that they correspond to increasing energy levels. The

Schrödinger equation governs the evolution of all energy levels in the state vector, including the guard levels, but the unitary gate transformation is only defined in the subspace of the essential states. This requirement leads us to define the target gate transformation matrix according to

$$V = \begin{bmatrix} V_g \\ \mathbf{0} \end{bmatrix} \in \mathbb{C}^{N \times E}, \quad V_g \in \mathbb{C}^{E \times E}, \quad V_g^\dagger V_g = I_E. \quad (6)$$

Let the state vector  $\psi_j(t, \boldsymbol{\alpha}) \in \mathbb{C}^N$  satisfy the Schrödinger equation,

$$\frac{d\psi_j}{dt} + iH(t, \boldsymbol{\alpha})\psi_j = 0, \quad 0 \leq t \leq T, \quad \psi_j(0, \boldsymbol{\alpha}) = \mathbf{e}_j, \quad (7)$$

for  $j = 0, 1, \dots, E-1$ . The solution operator matrix  $U(t, \boldsymbol{\alpha})$  and the target gate matrix  $V$  are rectangular with  $N$  rows and  $E$  columns,

$$U(t, \boldsymbol{\alpha}) = [\psi_0(t, \boldsymbol{\alpha}), \psi_1(t, \boldsymbol{\alpha}), \dots, \psi_{E-1}(t, \boldsymbol{\alpha})], \quad V = [\mathbf{d}_0, \mathbf{d}_1, \dots, \mathbf{d}_{E-1}]. \quad (8)$$

The decomposition (6) implies that the last  $G$  rows of  $\mathbf{d}_j$  must be zero.

The matrix overlap function  $R_V(U_T)$  in (2) generalizes in a straightforward way to unitary gates that are defined in the subspace, resulting in the target gate infidelity function

$$\mathcal{J}_1(U_T(\boldsymbol{\alpha})) = 1 - \frac{1}{E^2} |S_V(U_T(\boldsymbol{\alpha}))|^2, \quad S_V(U_T(\boldsymbol{\alpha})) = \sum_{j=0}^{E-1} \langle \psi_j(T, \boldsymbol{\alpha}), \mathbf{d}_j \rangle_2, \quad (9)$$

where  $\langle \cdot, \cdot \rangle_2$  is the  $\ell_2$  vector scalar product. The population of the guard states can be measured by the objective function

$$\mathcal{J}_2(U(\cdot, \boldsymbol{\alpha})) = \frac{1}{T} \int_0^T \sum_{j=0}^{E-1} \langle \psi_j(t, \boldsymbol{\alpha}), W \psi_j(t, \boldsymbol{\alpha}) \rangle_2 dt. \quad (10)$$

Here,  $W$  is a diagonal  $N \times N$  positive semi-definite weight matrix. The elements in  $W$  are zero for all essential states and are positive for the guard states. The elements of  $W$  are typically larger for higher energy levels in the model.

For the quantum control problem with guard states, we formulate the optimization problem as

$$\min_{\boldsymbol{\alpha}} \mathcal{G}(\boldsymbol{\alpha}) := \mathcal{J}_1(U_T(\boldsymbol{\alpha})) + \mathcal{J}_2(U(\cdot, \boldsymbol{\alpha})), \quad (11)$$

$$\frac{dU}{dt} + iH(t, \boldsymbol{\alpha})U = 0, \quad 0 \leq t \leq T, \quad U(0, \boldsymbol{\alpha}) = [\mathbf{e}_0, \mathbf{e}_1, \dots, \mathbf{e}_{E-1}]. \quad (12)$$

$$\alpha_{min} \leq \alpha_q \leq \alpha_{max}, \quad q = 1, 2, \dots, D. \quad (13)$$

In the special case of zero guard states,  $\mathcal{J}_2(U) = 0$  because  $W = 0$ . Thus, the above formulation applies to both the cases with and without guard states, i.e., when  $G = N - E \geq 0$ .

### 3. Real-valued formulation

A real-valued formulation of Schrödinger's equation (7) is given by

$$\begin{bmatrix} \dot{\mathbf{u}} \\ \dot{\mathbf{v}} \end{bmatrix} = \begin{bmatrix} S(t) & -K(t) \\ K(t) & S(t) \end{bmatrix} \begin{bmatrix} \mathbf{u} \\ \mathbf{v} \end{bmatrix} =: \begin{bmatrix} f^u(\mathbf{u}, \mathbf{v}, t) \\ f^v(\mathbf{u}, \mathbf{v}, t) \end{bmatrix}, \quad \begin{bmatrix} \mathbf{u}(0) \\ \mathbf{v}(0) \end{bmatrix} = \begin{bmatrix} \mathbf{g}^u \\ \mathbf{g}^v \end{bmatrix}, \quad (14)$$

where,

$$\mathbf{u} = \text{Re}(\boldsymbol{\psi}), \quad \mathbf{v} = -\text{Im}(\boldsymbol{\psi}), \quad K = \text{Re}(H), \quad S = \text{Im}(H),$$

Because the matrix  $H$  is Hermitian,  $K^T = K$  and  $S^T = -S$  (note that the matrix  $S$  is unrelated to the matrix overlap function  $S_V$ ). The real-valued formulation of Schrödinger's equation is a time-dependent Hamiltonian system corresponding to the Hamiltonian functional,

$$\mathcal{H}(\mathbf{u}, \mathbf{v}, t) = \mathbf{u}^T S(t) \mathbf{v} + \frac{1}{2} \mathbf{u}^T K(t) \mathbf{u} + \frac{1}{2} \mathbf{v}^T K(t) \mathbf{v}. \quad (15)$$

In general,  $S(t) \neq 0$ , which makes the Hamiltonian system non-separable.

In terms of the real-valued formulation, the columns of the solution operator matrix in (8) satisfy  $U = [\mathbf{u}_1 - i\mathbf{v}_1, \mathbf{u}_2 - i\mathbf{v}_2, \dots, \mathbf{u}_E - i\mathbf{v}_E]$ . Here,  $(\mathbf{u}_j, \mathbf{v}_j)$  satisfy (14) subject to the initial conditions  $\mathbf{g}_j^u = \mathbf{e}_j$  and  $\mathbf{g}_j^v = \mathbf{0}$ . The columns in the target gate matrix  $V$  correspond to

$$V = [\mathbf{d}_1^u - i\mathbf{d}_1^v, \mathbf{d}_2^u - i\mathbf{d}_2^v, \dots, \mathbf{d}_E^u - i\mathbf{d}_E^v], \quad \mathbf{d}_j^u = \text{Re}(\mathbf{d}_j), \quad \mathbf{d}_j^v = -\text{Im}(\mathbf{d}_j).$$

Using the real-valued notation, the objective function (11) can be written

$$\begin{aligned} \mathcal{G}(\boldsymbol{\alpha}) &= \left( 1 - \frac{1}{E^2} |S_V(U_T(\boldsymbol{\alpha}))|^2 \right) \\ &+ \frac{1}{T} \sum_{j=0}^{E-1} \int_0^T \left( \langle \mathbf{u}_j(t, \boldsymbol{\alpha}), W \mathbf{u}_j(t, \boldsymbol{\alpha}) \rangle_2 + \langle \mathbf{v}_j(t, \boldsymbol{\alpha}), W \mathbf{v}_j(t, \boldsymbol{\alpha}) \rangle_2 \right) dt, \quad (16) \end{aligned}$$

where,

$$\begin{aligned} S_V(U_T) &= \sum_{j=0}^{E-1} \left( \langle \mathbf{u}_j(T, \boldsymbol{\alpha}), \mathbf{d}_j^u \rangle_2 + \langle \mathbf{v}_j(T, \boldsymbol{\alpha}), \mathbf{d}_j^v \rangle_2 \right) \\ &+ i \sum_{j=0}^{E-1} \left( \langle \mathbf{v}_j(T, \boldsymbol{\alpha}), \mathbf{d}_j^u \rangle_2 - \langle \mathbf{u}_j(T, \boldsymbol{\alpha}), \mathbf{d}_j^v \rangle_2 \right). \quad (17) \end{aligned}$$

#### 3.1. Time integration

Let  $t_n = nh$ , for  $n = 0, 1, \dots, M$ , be a uniform grid in time where  $h = T/M$  is the time step. Also let  $\mathbf{u}^n \approx \mathbf{u}(t_n)$  and  $\mathbf{v}^n \approx \mathbf{v}(t_n)$  denote the numerical

solution on the grid. We use a partitioned Runge-Kutta (PRK) scheme [10] to discretize the real-valued formulation of Schrödinger's equation,

$$\mathbf{u}^0 = \mathbf{g}^u, \quad \mathbf{v}^0 = \mathbf{g}^v, \quad (18)$$

$$\mathbf{u}^{n+1} = \mathbf{u}^n + h \sum_{i=1}^s b_i^u \boldsymbol{\kappa}^{n,i}, \quad \mathbf{v}^{n+1} = \mathbf{v}^n + h \sum_{i=1}^s b_i^v \boldsymbol{\ell}^{n,i}, \quad (19)$$

$$\boldsymbol{\kappa}^{n,i} = f^u(\mathbf{U}^{n,i}, \mathbf{V}^{n,i}, t_n + c_i^u h), \quad \boldsymbol{\ell}^{n,i} = f^v(\mathbf{U}^{n,i}, \mathbf{V}^{n,i}, t_n + c_i^v h), \quad (20)$$

$$\mathbf{U}^{n,i} = \mathbf{u}^n + h \sum_{j=1}^s a_{ij}^u \boldsymbol{\kappa}^{n,j}, \quad \mathbf{V}^{n,i} = \mathbf{v}^n + h \sum_{j=1}^s a_{ij}^v \boldsymbol{\ell}^{n,j}. \quad (21)$$

Here,  $s \geq 1$  is the number of stages. The stage variables  $\mathbf{U}^{n,i}$  and  $\mathbf{V}^{n,i}$  are set in a bold font to indicate that they are unrelated to the solution operator matrix  $U(t, \boldsymbol{\alpha})$  and the target gate matrix  $V$ .

The Störmer-Verlet scheme is a two-stage PRK method ( $s = 2$ ) that is symplectic, time-reversible and second order accurate [10]. It combines the trapezoidal and the implicit midpoint rules, with Butcher coefficients:

$$a_{11}^u = a_{12}^u = 0, \quad a_{21}^u = a_{22}^u = \frac{1}{2}, \quad a_{11}^v = a_{21}^v = \frac{1}{2}, \quad a_{12}^v = a_{22}^v = 0, \quad (22)$$

$$b_1^u = b_2^u = \frac{1}{2}, \quad c_1^u = 0, \quad c_2^u = 1, \quad b_1^v = b_2^v = \frac{1}{2}, \quad c_1^v = c_2^v = \frac{1}{2}. \quad (23)$$

### 3.2. Time step restrictions for accuracy and stability

The accuracy in the numerical solution of Schrödinger's equation is essentially determined by how well the fastest time scale in the state vector is resolved on the grid in time. The analysis of the time scales in the solution of Schrödinger's equation is most straightforward to perform in the complex-valued formulation (7).

There are two fundamental time scales that must be resolved in the solution of Schrödinger's equation. The first corresponds to how quickly the control functions must vary in time to trigger the desired transitions between the energy levels in the quantum system. This time scale is determined by the transition frequencies in the system Hamiltonian, which follow as the difference between its consecutive eigenvalues. In the Hamiltonian model (4), the angular transition frequencies between the essential energy levels are

$$\Delta_j = j\xi_a, \quad j = 0, \dots, E-1. \quad (24)$$

The second time scale is due to the harmonic oscillation of the phase in the state vector. It can be estimated by freezing the time-dependent coefficients in the Hamiltonian matrix at some time  $t = t_*$  and considering Schrödinger's equation with the time-independent Hamiltonian matrix  $H_* = H(t_*)$ . The  $N \times N$  matrix  $H_*$  is Hermitian and can be diagonalized by a unitary transformation,

$$H_* X = X \Gamma, \quad X^\dagger X = I_N, \quad \Gamma = \text{diag}(\gamma_1, \gamma_2, \dots, \gamma_N),$$

where the eigenvalues  $\gamma_k$  are real. By the change of variables  $\tilde{\psi} = X^\dagger \psi$ , the solution of the diagonalized system follows as

$$\tilde{\psi}_k(t) = e^{-i\gamma_k t} \tilde{\psi}_k(0),$$

corresponding to the period  $\tau_k = 2\pi/|\gamma_k|$ . The shortest period thus follows from the spectral radius of  $H_*$ ,  $\rho(H_*) = \max_k |\gamma_k|$ .

To estimate the time step for the Störmer-Verlet method, we require that the shortest period in the solution of Schrödinger's equation must be resolved by at least  $C_P$  time steps. Taking both time scales into account leads to the time step restriction

$$h \leq \frac{2\pi}{C_P \max\{\rho(H_*), \max_j (|\Delta_j|)\}}. \quad (25)$$

The value of  $C_P$  that is needed to obtain a given accuracy in the numerical solution depends on the order of accuracy, the duration of the time integration, as well as the details of the time-stepping scheme. For second order accurate methods such as the Störmer-Verlet method, acceptable accuracy for engineering applications can often be achieved with  $C_P \approx 40$ . With the Störmer-Verlet method, we note that the time-stepping can become unstable if  $C_P \leq 2$ , corresponding to a sampling rate below the Nyquist limit.

After freezing the coefficients, the Hamiltonian (4) becomes

$$H_* = -\frac{\xi_a}{2} a^\dagger a^\dagger a a + p_*(a + a^\dagger) + iq_*(a - a^\dagger), \quad p_* = p(t_*, \boldsymbol{\alpha}), \quad q_* = q(t_*, \boldsymbol{\alpha}).$$

We can estimate the spectral radius of  $H_* \in \mathbb{C}^{N \times N}$  using the Gershgorin circle theorem [8]. Because  $H_*$  is Hermitian, all its eigenvalues are real. As a result, its spectral radius can be bounded by

$$\rho(H_*) \leq \frac{|\xi_a|}{2} (N-1)(N-2) + (|p_*| + |q_*|) \sqrt{N-1}.$$

Hence, it is the largest value of  $(|p_*| + |q_*|)$  that determines the time step.

Given the parameter vector  $\boldsymbol{\alpha}$ , the control functions are bounded by  $p_\infty = \max_t |p(t, \boldsymbol{\alpha})|$  and  $q_\infty = \max_t |q(t, \boldsymbol{\alpha})|$ , where the maximum is evaluated for times  $0 \leq t \leq T$ . Thus, using the estimate

$$\rho(H_*) \leq \frac{|\xi_a|}{2} (N-1)(N-2) + (p_\infty + q_\infty) \sqrt{N-1}, \quad (26)$$

in (25) guarantees that the time-dependent phase in the state vector is resolved by at least  $C_P$  time steps per shortest period.

If the optimization imposes amplitude constraints on the parameter vector,  $|\boldsymbol{\alpha}|_\infty \leq \alpha_{max}$ , those constraints can be used to estimate the time step before the optimization starts. This allows the same time step to be used throughout the iteration and eliminates the need to recalculate the spectral radius of  $H_*$  when  $\boldsymbol{\alpha}$  changes.

Our implementation of the Störmer-Verlet scheme was verified to be second order accurate. It was also found to give approximately the same accuracy as the second order Magnus integrator [10] when the same time step was used in both methods (data not shown to conserve space).

#### 4. Discretizing the objective function and its gradient

In this section, we develop a “discretize before optimize” approach in which we first discretize the objective function and then derive a compatible scheme for discretizing the adjoint state equation, which is used for computing the gradient of the objective function. As was outlined in the introduction, our approach builds upon the works of Hager [9], Sanz-Serna [19] and Ober-Blöbaum [18].

##### 4.1. Discretizing the objective function

The Störmer-Verlet scheme can be written in terms of the stage variables  $(\mathbf{U}^{n,i}, \mathbf{V}^{n,i})$  by substituting  $(\boldsymbol{\kappa}^{n,i}, \boldsymbol{\ell}^{n,i})$  from (20) into (19),

$$\mathbf{u}^0 = \mathbf{g}^u, \quad \mathbf{v}^0 = \mathbf{g}^v, \quad (27)$$

$$\mathbf{u}^{n+1} = \mathbf{u}^n + \frac{h}{2} (S_n \mathbf{U}^{n,1} + S_{n+1} \mathbf{U}^{n,2} - K_n \mathbf{V}^{n,1} - K_{n+1} \mathbf{V}^{n,2}), \quad (28)$$

$$\mathbf{v}^{n+1} = \mathbf{v}^n + \frac{h}{2} (K_{n+1/2} (\mathbf{U}^{n,1} + \mathbf{U}^{n,2}) + S_{n+1/2} (\mathbf{V}^{n,1} + \mathbf{V}^{n,2})), \quad (29)$$

and into (21),

$$\mathbf{U}^{n,1} = \mathbf{u}^n, \quad (30)$$

$$\mathbf{U}^{n,2} = \mathbf{u}^n + \frac{h}{2} (S_n \mathbf{U}^{n,1} + S_{n+1} \mathbf{U}^{n,2} - K_n \mathbf{V}^{n,1} - K_{n+1} \mathbf{V}^{n,2}), \quad (31)$$

$$\mathbf{V}^{n,1} = \mathbf{v}^n + \frac{h}{2} (K_{n+1/2} \mathbf{U}^{n,1} + S_{n+1/2} \mathbf{V}^{n,1}), \quad (32)$$

$$\mathbf{V}^{n,2} = \mathbf{v}^n + \frac{h}{2} (K_{n+1/2} \mathbf{U}^{n,1} + S_{n+1/2} \mathbf{V}^{n,1}). \quad (33)$$

Here,  $S_n = S(t_n)$ ,  $S_{n+1/2} = S(t_n + 0.5h)$ , etc. Because  $S(t) \neq 0$ , the scheme is block implicit. Note that  $\mathbf{u}^{n+1} = \mathbf{U}^{n,2}$  and  $\mathbf{V}^{n,1} = \mathbf{V}^{n,2} = \mathbf{v}(t_{n+1/2}) + \mathcal{O}(h^2)$ .

The numerical solution at the final time step provides a second order accurate approximation of the continuous solution operator matrix  $U_T$ , which we denote  $U_{Th}$ . It is used to approximate the matrix overlap function  $S_V(U_T)$  in (17),

$$S_{Vh}(U_{Th}) = \sum_{j=0}^{E-1} \left( \langle \mathbf{u}_j^M, \mathbf{d}_j^u \rangle_2 + \langle \mathbf{v}_j^M, \mathbf{d}_j^v \rangle_2 \right) + i \sum_{j=0}^{E-1} \left( \langle \mathbf{v}_j^M, \mathbf{d}_j^u \rangle_2 - \langle \mathbf{u}_j^M, \mathbf{d}_j^v \rangle_2 \right), \quad (34)$$

which is then used as the first part of the discrete objective function,

$$\mathcal{J}_{1h}(U_{Th}) = \left( 1 - \frac{1}{E^2} |S_{Vh}(U_{Th})|^2 \right). \quad (35)$$

The integral in the objective function (16) can be discretized to second order accuracy by using the Runge-Kutta stage variables,

$$\mathcal{J}_{2h}(\mathbf{U}, \mathbf{V}) = \frac{h}{T} \sum_{j=0}^{E-1} \sum_{n=0}^{M-1} \left( \frac{1}{2} \langle \mathbf{U}_j^{n,1}, W \mathbf{U}_j^{n,1} \rangle_2 + \frac{1}{2} \langle \mathbf{U}_j^{n,2}, W \mathbf{U}_j^{n,2} \rangle_2 + \langle \mathbf{V}_j^{n,1}, W \mathbf{V}_j^{n,1} \rangle_2 \right). \quad (36)$$

Based on the above formulas we discretize the objective function (16) according to

$$\mathcal{G}_h(\boldsymbol{\alpha}) = \mathcal{J}_h(U_{Th}^\alpha, \mathbf{U}^\alpha, \mathbf{V}^\alpha), \quad \mathcal{J}_h(U_{Th}, \mathbf{U}, \mathbf{V}) := \mathcal{J}_{1h}(U_{Th}) + \mathcal{J}_{2h}(\mathbf{U}, \mathbf{V}). \quad (37)$$

Here,  $U_{Th}^\alpha$ ,  $\mathbf{U}^\alpha$  and  $\mathbf{V}^\alpha$  represent the time-discrete solution of the Störmer-Verlet scheme for a given parameter vector  $\boldsymbol{\alpha}$ . We note that  $\mathcal{G}_h(\boldsymbol{\alpha})$  can be evaluated by accumulation during the time-stepping of the Störmer-Verlet scheme.

#### 4.2. The discrete adjoint approach

The gradient of the discretized objective function can be derived from first order optimality conditions of the corresponding discrete Lagrangian. In this approach, let  $(\boldsymbol{\mu}_j^n, \boldsymbol{\nu}_j^n)$  be the adjoint variables and let  $(\mathbf{M}_j^{n,i}, \mathbf{N}_j^{n,i})$  be Lagrange multipliers. We define the discrete Lagrangian by

$$\mathcal{L}_h(\mathbf{u}, \mathbf{v}, \mathbf{U}, \mathbf{V}, \boldsymbol{\mu}, \boldsymbol{\nu}, \mathbf{M}, \mathbf{N}, \boldsymbol{\alpha}) = \mathcal{J}_h(U_{Th}, \mathbf{U}, \mathbf{V}) - \sum_{j=0}^{E-1} \left( \langle \mathbf{u}_j^0 - \mathbf{g}_j^u, \boldsymbol{\mu}_j^0 \rangle_2 + \langle \mathbf{v}_j^0 - \mathbf{g}_j^v, \boldsymbol{\nu}_j^0 \rangle_2 + \sum_{k=1}^6 T_j^k \right). \quad (38)$$

The first two terms in the sum enforce the initial conditions (27). The terms  $T_j^1$  and  $T_j^2$  enforce the time-stepping update formulas (28)-(29) in the Störmer-Verlet scheme,

$$T_j^1 = \sum_{n=0}^{M-1} \left\langle \mathbf{u}_j^{n+1} - \mathbf{u}_j^n - \frac{h}{2} \left( S_n \mathbf{U}_j^{n,1} + S_{n+1} \mathbf{U}_j^{n,2} - K_n \mathbf{V}_j^{n,1} - K_{n+1} \mathbf{V}_j^{n,2} \right), \boldsymbol{\mu}_j^{n+1} \right\rangle_2, \quad (39)$$

$$T_j^2 = \sum_{n=0}^{M-1} \left\langle \mathbf{v}_j^{n+1} - \mathbf{v}_j^n - \frac{h}{2} \left( K_{n+1/2} \left( \mathbf{U}_j^{n,1} + \mathbf{U}_j^{n,2} \right) + S_{n+1/2} \left( \mathbf{V}_j^{n,1} + \mathbf{V}_j^{n,2} \right) \right), \boldsymbol{\nu}_j^{n+1} \right\rangle_2. \quad (40)$$

The terms  $T_j^3$  to  $T_j^6$  enforce the relations between the stage variables (30)-(33) using the Lagrange multipliers  $(\mathbf{M}_j^{n,i}$  and  $\mathbf{N}_j^{n,i})$ , see Appendix B for details.

To derive the discrete adjoint scheme, we note that the discrete Lagrangian (38) has a saddle point if

$$\frac{\partial \mathcal{L}_h}{\partial \boldsymbol{\mu}_j^n} = \frac{\partial \mathcal{L}_h}{\partial \boldsymbol{\nu}_j^n} = \frac{\partial \mathcal{L}_h}{\partial \mathbf{N}_j^{n,i}} = \frac{\partial \mathcal{L}_h}{\partial \mathbf{M}_j^{n,i}} = 0, \quad (41)$$

$$\frac{\partial \mathcal{L}_h}{\partial \mathbf{u}_j^n} = \frac{\partial \mathcal{L}_h}{\partial \mathbf{v}_j^n} = \frac{\partial \mathcal{L}_h}{\partial \mathbf{U}_j^{n,i}} = \frac{\partial \mathcal{L}_h}{\partial \mathbf{V}_j^{n,i}} = 0, \quad (42)$$

for  $n = 0, 1, \dots, M$ ,  $i = 1, 2$  and  $j = 0, 1, \dots, E-1$ . Here, the set of conditions in (41) result in the Störmer-Verlet scheme (27)-(33) for evolving  $(\mathbf{u}_j^n, \mathbf{v}_j^n, \mathbf{U}_j^{n,i}, \mathbf{V}_j^{n,i})$  forwards in time. The set of conditions in (42) result in a time-stepping scheme for evolving the adjoint variables  $(\boldsymbol{\mu}_j^n, \boldsymbol{\nu}_j^n)$  backwards in time, as is made precise in the following lemma.

**Lemma 1.** *Let  $\mathcal{L}_h$  be the discrete Lagrangian defined by (38). Furthermore, let  $(\mathbf{u}_j^n, \mathbf{v}_j^n, \mathbf{U}_j^{n,i}, \mathbf{V}_j^{n,i})$  satisfy the Störmer-Verlet scheme (27)-(33) for a given parameter vector  $\boldsymbol{\alpha}$ . Then, the set of saddle-point conditions (42) are satisfied if the Lagrange multipliers  $(\boldsymbol{\mu}_j^n, \boldsymbol{\nu}_j^n)$  are calculated according to the reversed time-stepping scheme,*

$$\boldsymbol{\mu}_j^M = \frac{\partial \mathcal{J}_h}{\partial \mathbf{u}_j^M}, \quad \boldsymbol{\nu}_j^M = \frac{\partial \mathcal{J}_h}{\partial \mathbf{v}_j^M}, \quad (43)$$

$$\boldsymbol{\mu}_j^n = \boldsymbol{\mu}_j^{n+1} - \frac{h}{2} (\boldsymbol{\kappa}_j^{n,1} + \boldsymbol{\kappa}_j^{n,2}), \quad (44)$$

$$\boldsymbol{\nu}_j^n = \boldsymbol{\nu}_j^{n+1} - \frac{h}{2} (\boldsymbol{\ell}_j^{n,1} + \boldsymbol{\ell}_j^{n,2}), \quad (45)$$

for  $n = M-1, M-2, \dots, 0$ . Because  $S^T = -S$  and  $K^T = K$ , the slopes satisfy

$$\boldsymbol{\kappa}_j^{n,1} = S_n \mathbf{X}_j^n - K_{n+1/2} \mathbf{Y}_j^{n,1} - \frac{2}{h} \frac{\partial \mathcal{J}_h}{\partial \mathbf{U}_j^{n,1}}, \quad (46)$$

$$\boldsymbol{\kappa}_j^{n,2} = S_{n+1} \mathbf{X}_j^n - K_{n+1/2} \mathbf{Y}_j^{n,2} - \frac{2}{h} \frac{\partial \mathcal{J}_h}{\partial \mathbf{U}_j^{n,2}}, \quad (47)$$

$$\boldsymbol{\ell}_j^{n,1} = K_n \mathbf{X}_j^n + S_{n+1/2} \mathbf{Y}_j^{n,1} - \frac{2}{h} \frac{\partial \mathcal{J}_h}{\partial \mathbf{V}_j^{n,1}}, \quad (48)$$

$$\boldsymbol{\ell}_j^{n,2} = K_{n+1} \mathbf{X}_j^n + S_{n+1/2} \mathbf{Y}_j^{n,2} - \frac{2}{h} \frac{\partial \mathcal{J}_h}{\partial \mathbf{V}_j^{n,2}}, \quad (49)$$

where the stage variables are given by

$$\mathbf{X}_j^n = \boldsymbol{\mu}_j^{n+1} - \frac{h}{2} \boldsymbol{\kappa}_j^{n,2}, \quad (50)$$

$$\mathbf{Y}_j^{n,2} = \boldsymbol{\nu}_j^{n+1}, \quad (51)$$

$$\mathbf{Y}_j^{n,1} = \boldsymbol{\nu}_j^{n+1} - \frac{h}{2} (\boldsymbol{\ell}_j^{n,1} + \boldsymbol{\ell}_j^{n,2}). \quad (52)$$

*Proof.* The lemma follows after a somewhat tedious but straightforward calculation shown in detail in Appendix B.  $\square$

Corresponding to the continuous Schrödinger equation (14), the adjoint state equation (without forcing) is

$$\begin{bmatrix} \dot{\boldsymbol{\mu}} \\ \dot{\boldsymbol{\nu}} \end{bmatrix} = \begin{bmatrix} S(t) & -K(t) \\ K(t) & S(t) \end{bmatrix} \begin{bmatrix} \boldsymbol{\mu} \\ \boldsymbol{\nu} \end{bmatrix} =: \begin{bmatrix} \mathbf{f}^\mu(\boldsymbol{\mu}, \boldsymbol{\nu}, t) \\ \mathbf{f}^\nu(\boldsymbol{\mu}, \boldsymbol{\nu}, t) \end{bmatrix}, \quad (53)$$

where we used that  $S^T = -S$  and  $K^T = K$ .

**Corollary 1.** *The time-stepping scheme (44)-(52) (without forcing) is a consistent approximation of the continuous adjoint state equation (53). It can be written as a modified partitioned Runge-Kutta method, where the Butcher coefficients are*

$$a_{11}^\mu = a_{21}^\mu = 1/2, \quad a_{12}^\mu = a_{22}^\mu = 0, \quad a_{11}^\nu = a_{12}^\nu = 0, \quad a_{21}^\nu = a_{22}^\nu = 1/2, \quad (54)$$

$$b_1^\mu = b_2^\mu = \frac{1}{2}, \quad b_1^\nu = b_2^\nu = \frac{1}{2}, \quad (55)$$

corresponding to the implicit midpoint rule for the  $\boldsymbol{\mu}$ -equation and the trapezoidal rule for the  $\boldsymbol{\nu}$ -equation in (53). The modifications to the partitioned Runge-Kutta scheme concerns the formulae for the slopes, (46)-(49). Because of the time-levels at which the matrices  $K$  and  $S$  are evaluated, it is not possible to define Butcher coefficients  $c_i^\mu$  and  $c_i^\nu$  such that

$$\begin{aligned} \boldsymbol{\kappa}_j^{n,i} &= \mathbf{f}^\mu(\mathbf{X}_j^{n,i}, \mathbf{Y}_j^{n,i}, t_n + c_i^\mu h), \\ \boldsymbol{\ell}_j^{n,i} &= \mathbf{f}^\nu(\mathbf{X}_j^{n,i}, \mathbf{Y}_j^{n,i}, t_n + c_i^\nu h). \end{aligned}$$

*Proof.* See Appendix C.  $\square$

Only the matrices  $K$  and  $S$  depend explicitly on  $\boldsymbol{\alpha}$  in the discrete Lagrangian. When the saddle point conditions (41) and (42) are satisfied, we can therefore calculate the gradient of  $\mathcal{G}_h$  by differentiating (38),

$$\frac{\partial \mathcal{G}_h}{\partial \alpha_r} = \frac{\partial \mathcal{L}_h}{\partial \alpha_r}, \quad r = 0, 1, \dots, E-1.$$

This relation leads to the following lemma.

**Lemma 2.** *Let  $\mathcal{L}_h$  be the discrete Lagrangian defined by (38). Assume that  $(\mathbf{u}_j^n, \mathbf{v}_j^n, \mathbf{U}_j^{n,i}, \mathbf{V}_j^{n,i})$  are calculated according to the Störmer-Verlet scheme for a given parameter vector  $\boldsymbol{\alpha}$ . Furthermore, assume that  $(\boldsymbol{\mu}_j^n, \boldsymbol{\nu}_j^n, \mathbf{X}_j^n, \mathbf{Y}_j^{n,i})$  satisfy the adjoint time-stepping scheme in Lemma 1, subject to the terminal conditions*

$$\boldsymbol{\mu}_j^M = -\frac{2}{E^2} (\operatorname{Re}(S_{Vh})\mathbf{d}_j^u - \operatorname{Im}(S_{Vh})\mathbf{d}_j^v), \quad \boldsymbol{\nu}_j^M = -\frac{2}{E^2} (\operatorname{Re}(S_{Vh})\mathbf{d}_j^v + \operatorname{Im}(S_{Vh})\mathbf{d}_j^u),$$

and the forcing functions

$$\begin{aligned}\frac{\partial \mathcal{J}_h}{\partial \mathbf{U}_j^{n,1}} &= \frac{h}{T} W \mathbf{U}_j^{n,1}, & \frac{\partial \mathcal{J}_h}{\partial \mathbf{U}_j^{n,2}} &= \frac{h}{T} W \mathbf{U}_j^{n,2} \\ \frac{\partial \mathcal{J}_h}{\partial \mathbf{V}_j^{n,1}} &= \frac{h}{T} W \mathbf{V}_j^{n,1}, & \frac{\partial \mathcal{J}_h}{\partial \mathbf{V}_j^{n,2}} &= 0.\end{aligned}$$

Then, the saddle-point conditions (41) and (42) are satisfied and the gradient of the objective function (37) is given by

$$\begin{aligned}\frac{\partial \mathcal{G}_h}{\partial \alpha_r} &= \frac{h}{2} \sum_{j=0}^{E-1} \sum_{n=0}^{M-1} \left\{ \left\langle S'_n \mathbf{U}_j^{n,1} + S'_{n+1} \mathbf{U}_j^{n,2} - (K'_n + K'_{n+1}) \mathbf{V}_j^{n,1}, \mathbf{X}_j^n \right\rangle_2 \right. \\ &\quad \left. + \left\langle K'_{n+1/2} \mathbf{U}_j^{n,1} + S'_{n+1/2} \mathbf{V}_j^{n,1}, \mathbf{Y}_j^{n,1} \right\rangle_2 + \left\langle K'_{n+1/2} \mathbf{U}_j^{n,2} + S'_{n+1/2} \mathbf{V}_j^{n,1}, \mathbf{Y}_j^{n,2} \right\rangle_2 \right\},\end{aligned}\tag{56}$$

where  $S'_n = \partial S / \partial \alpha_r(t_n)$ ,  $K'_{n+1/2} = \partial K / \partial \alpha_r(t_{n+1/2})$ , etc.

*Proof.* See Appendix D.  $\square$

As a result of Lemma 2, all components of the gradient can be calculated from  $(\mathbf{u}_j^n, \mathbf{v}_j^n, \mathbf{U}_j^{n,i}, \mathbf{V}_j^{n,1})$  and the adjoint variables  $(\boldsymbol{\mu}_j^n, \boldsymbol{\nu}_j^n, \mathbf{X}_j^n, \mathbf{Y}_j^{n,i})$ . The first set of variables are obtained from time-stepping the Störmer-Verlet scheme forward in time, while the second set of variables follow from time-stepping the adjoint scheme backward in time.

We can avoid storing the time-history of  $(\mathbf{u}_j^n, \mathbf{v}_j^n, \mathbf{U}_j^{n,i}, \mathbf{V}_j^{n,1})$  by using the time-reversibility of the Störmer-Verlet scheme. However, in order to do so, we must first calculate the terminal conditions  $(\mathbf{u}_j^M, \mathbf{v}_j^M)$  by evolving (27)-(33) forwards in time. The time-stepping can then be reversed and the gradient of the objective function (56) can be accumulated by simultaneously time-stepping the adjoint system (44)-(52) backwards in time.

## 5. Quadratic B-splines with carrier waves

Let  $A(t)$  and  $\phi(t)$  be real-valued amplitude and phase functions of time. By taking the control functions in the rotating frame Hamiltonian (4) to be

$$p(t) = A(t) \cos(\phi(t)), \quad q(t) = A(t) \sin(\phi(t)),$$

the relation (5) results in the laboratory frame control function

$$f(t) = 2A(t) \cos(\omega_a t + \phi(t)).\tag{57}$$

We expand the amplitude function in a set of basis functions  $\{B_k\}_{k=1}^{D_1}$  and start by considering the case of one carrier wave. We make the ansatz,

$$A(t) = \sum_{k=1}^{D_1} B_k(t) \beta_k,$$

where  $\beta_k$  are real coefficients. By defining the phase as  $\phi_k(t) = \Omega t + \theta_k$ ,

$$\begin{aligned} p(t) &= \sum_{k=1}^{D_1} B_k(t) \beta_k \cos(\Omega t + \theta_k) = \sum_{k=1}^{D_1} B_k(t) \left[ \alpha_k^{(1)} \cos(\Omega t) - \alpha_k^{(2)} \sin(\Omega t) \right], \\ q(t) &= \sum_{k=1}^{D_1} B_k(t) \beta_k \sin(\Omega t + \theta_k) = \sum_{k=1}^{D_1} B_k(t) \left[ \alpha_k^{(1)} \sin(\Omega t) + \alpha_k^{(2)} \cos(\Omega t) \right]. \end{aligned}$$

where

$$\alpha_k^{(1)} = \beta_k \cos(\theta_k), \quad \alpha_k^{(2)} = \beta_k \sin(\theta_k).$$

In the laboratory frame, the resulting control function becomes

$$f(t) = 2 \sum_{k=1}^{D_1} B_k(t) \beta_k \cos((\omega_a + \Omega)t + \theta_k).$$

The case with one carrier wave is straightforward to generalize to multiple frequencies,  $\{\Omega_\ell\}_{\ell=1}^{N_f}$ . This leads to a laboratory frame control function with a spectrum that can be precisely specified to match the transition frequencies of the system,

$$f(t) = 2 \sum_{\ell=1}^{N_f} \sum_{k=1}^{D_1} B_k(t) \beta_{k,\ell} \cos((\omega_a + \Omega_\ell)t + \theta_{k,\ell}).$$

The total number of control parameters becomes  $D = 2N_f D_1$ , which equals the size of the parameter vector  $\boldsymbol{\alpha}$ . Here,  $N_f$  is the number of frequencies and  $D_1 \geq 1$  is the number of basis functions per frequency.

In this paper we use the quadratic B-spline basis (see Figure 1) to represent the amplitude and phase of the control functions. Here, each basis function is a piecewise quadratic polynomial in time. It is the lowest order B-spline function that has at least one continuous derivative. We define the basis functions on a uniform grid in time,

$$t_m = (m - 1.5)\delta, \quad m = 1, \dots, D_1, \quad \delta = \frac{T}{D_1 - 2}. \quad (58)$$

Each basis function  $B_m(t)$  is centered around  $t = t_m$  and is easily expressed in terms of the scaled time parameter  $\tau_m(t) = (t - t_m)/3\delta$ ,

$$B_m(t) = \tilde{B}(\tau_m(t)), \quad \tilde{B}(\tau) = \begin{cases} \frac{9}{8} + \frac{9}{2}\tau + \frac{9}{2}\tau^2, & -\frac{1}{2} \leq \tau < -\frac{1}{6}, \\ \frac{3}{4} - 9\tau^2, & -\frac{1}{6} \leq \tau < \frac{1}{6}, \\ \frac{9}{8} - \frac{9}{2}\tau + \frac{9}{2}\tau^2, & \frac{1}{6} \leq \tau < \frac{1}{2}, \\ 0, & \text{otherwise.} \end{cases} \quad (59)$$

Note that  $B_m(t)$  is only non-zero in the interval  $t \in [t_m - 1.5\delta, t_m + 1.5\delta]$ . Thus, for any fixed time  $t$ , a control function will only get contributions from at most three B-spline basis functions. This property allows the control functions to be evaluated very efficiently.

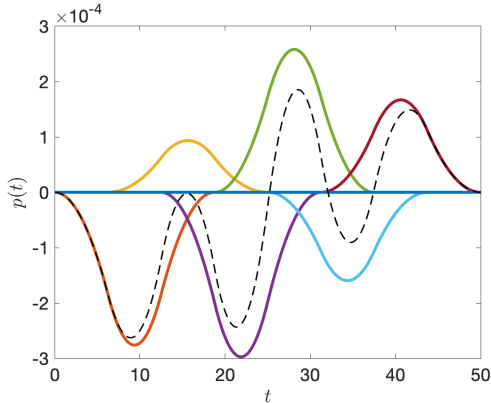


Figure 2: A B-spline control function  $p(t, \alpha)$  without carrier wave ( $\Omega_1 = 0$  and  $N_f = 1$ ). Here, the black dashed line is the control function and the solid colored lines are the individual B-spline basis functions, scaled by  $\alpha_{m,1}^1$ . In this case,  $D_1 = 6$ .

## 6. Numerical optimization

Our numerical solution of the optimal control problem is based on the general purpose interior-point optimization package IPOPT [21]. This open-source library implements a primal-dual barrier approach for solving large-scale nonlinear programming problems, i.e., it minimizes an objective function subject to inequality (barrier) constraints on the parameter vector. Because the Hessian of the objective function is costly to calculate, we use the L-BFGS algorithm [17] in IPOPT, which only relies on the objective function and its gradient to be evaluated. Inequality constraints that limit the amplitude of the parameter vector  $\alpha$  are enforced internally by IPOPT.

The routines for evaluating the objective function and its gradient are implemented in the Julia programming language [2], which provides a convenient interface to IPOPT. Given a parameter vector  $\alpha$ , the routine for evaluating the objective function solves the Schrödinger equation with the Störmer-Verlet scheme and evaluates  $\mathcal{G}_h(\alpha)$  by accumulation. The routine for evaluating the gradient first applies the Störmer-Verlet scheme to calculate terminal conditions for the state variables. It then proceeds by accumulating the gradient  $\nabla_{\alpha} \mathcal{G}_h$  by simultaneous reversed time-stepping of the discrete adjoint scheme and the Störmer-Verlet scheme. These two fundamental routines, together with functions for setting up the Hamiltonians, estimating the time step, setting up constraints on the parameter vector, post-processing and plotting of the results have been implemented in the software package JuQBox, which was used to generate the numerical results below.

The adjoint gradient implementation has been verified against a centered finite difference approximation of the discrete objective function by perturbing each component of the parameter vector. To further verify our implementation, we also calculated the discrete gradient by differentiating the Störmer-Verlet

scheme with respect to each component of the parameter vector. This gradient agreed with the adjoint gradient to within 11-12 digits. (Data not shown to conserve space.)

### 6.1. A CNOT gate on a single qudit with guard levels

To test our methods on a quantum optimal control problem, we consider realizing a CNOT gate on a single qudit with four essential energy levels and two guard levels. The qudit is modeled in the rotating frame of reference using the Hamiltonian (4) with fundamental frequency  $\omega_a/2\pi = 4.10336$  GHz and self-Kerr coefficient  $\xi_a/2\pi = 0.2198$  GHz. We parameterize the two control functions using B-splines with carrier waves and choose the frequencies to be  $\Omega_1 = 0$ ,  $\Omega_2 = -\xi_a$  and  $\Omega_3 = -2\xi_a$ . In the rotating frame, these frequencies correspond to transitions between the ground state and the first excited state, the first and second excited states and the second and third excited states. We discourage population of the fourth and fifth excited states using the weight matrix  $W = \text{diag}[0, 0, 0, 0, 0.1, 1.0]$  in  $\mathcal{J}_{2h}$ , see (10). We use  $D_1 = 10$  basis functions per frequency and control function, resulting in a total of  $D = 60$  parameters. The amplitudes of the control functions are limited by the constraint

$$\|\boldsymbol{\alpha}\|_\infty := \max_{1 \leq r \leq D} |\alpha_r| \leq \alpha_{max}. \quad (60)$$

We set the gate duration to  $T = 100$  ns and estimate the time step using the technique in Section 3.2. To guarantee at least  $C_P = 40$  time steps per period, we use  $M = 8,796$  time steps, corresponding to  $h \approx 1.136 \cdot 10^{-2}$  ns.

As initial guess for the elements of the parameter vector, we use a random number generator with a uniform distribution in  $[-0.01, 0.01]$ . In Figure 3 we present the convergence history with the two parameter thresholds  $\alpha_{max}/2\pi = 4$  MHz and 3 MHz, respectively. We show the objective function  $\mathcal{G}$ , decomposed into  $\mathcal{J}_{1h}$  and  $\mathcal{J}_{2h}$ , together with the norm of the dual infeasibility,  $\|\nabla_\alpha \mathcal{G} - z\|_\infty$ , that IPOPT uses to monitor convergence, see [21] for details. For the case with  $\alpha_{max}/2\pi = 3$  MHz, IPOPT converges well and needs 126 iteration to reduce the dual infeasibility to  $10^{-5}$ , which was used as convergence criteria. However, when the parameter constraint is relaxed to  $\alpha_{max}/2\pi = 4$  MHz, the convergence of IPOPT stalls after about 100 iterations and is terminated after 200 iterations.

For the converged solution with parameter constraint  $\alpha_{max}/2\pi = 3$  MHz, the two parts of the objective function are  $\mathcal{J}_{1h} \approx 1.47 \cdot 10^{-4}$  and  $\mathcal{J}_{2h} \approx 4.72 \cdot 10^{-5}$ , corresponding to a trace fidelity greater than 0.9998. The population of the guard states remains small for all times and initial conditions. In particular, the “forbidden” state  $|5\rangle$  has a population that remains below  $4.04 \cdot 10^{-7}$ , see Figure 4. The optimized control functions are shown in Figure 5 and the population of the essential states, corresponding to the four initial conditions of the CNOT gate, are presented in Figure 6.

Even though the dual infidelity does not reach the convergence criteria with the parameter threshold  $\alpha_{max}/2\pi = 4$  MHz, the resulting control functions give a very small objective function. Here,  $\mathcal{J}_{1h} \approx 8.56 \cdot 10^{-5}$  and  $\mathcal{J}_{2h} \approx 4.15 \cdot 10^{-5}$ ,

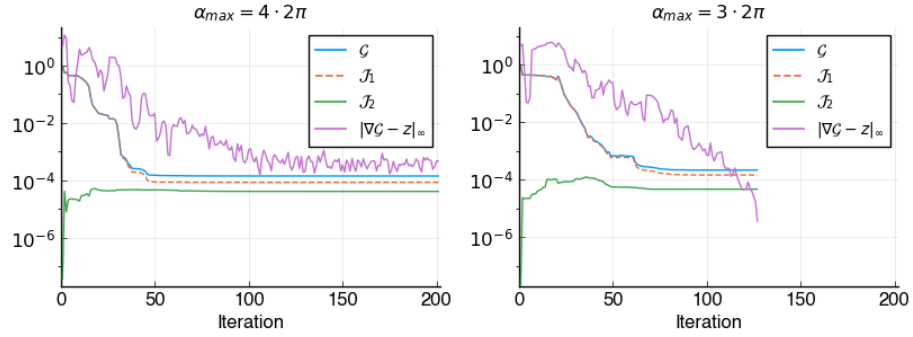


Figure 3: Convergence of the IPOPT iteration for the CNOT gate with the parameter constraint  $\|\alpha\|_\infty \leq \alpha_{max}$ . Here,  $\alpha_{max}/2\pi = 4$  MHz (left) and  $\alpha_{max}/2\pi = 3$  MHz (right).

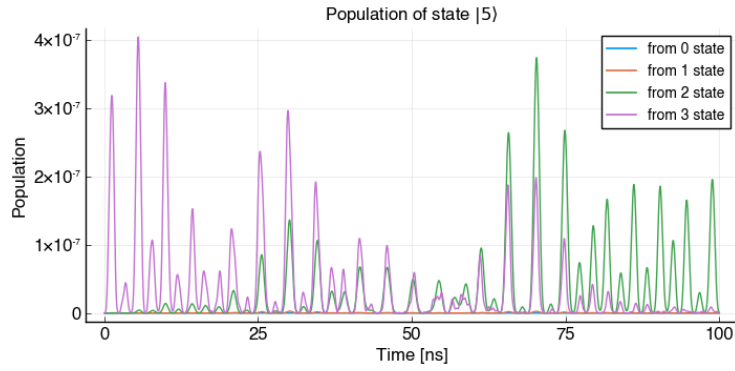


Figure 4: The population of the “forbidden” state  $|5\rangle$  as function of time for the four initial conditions of the CNOT gate. Here,  $\alpha_{max}/2\pi = 3$  MHz.

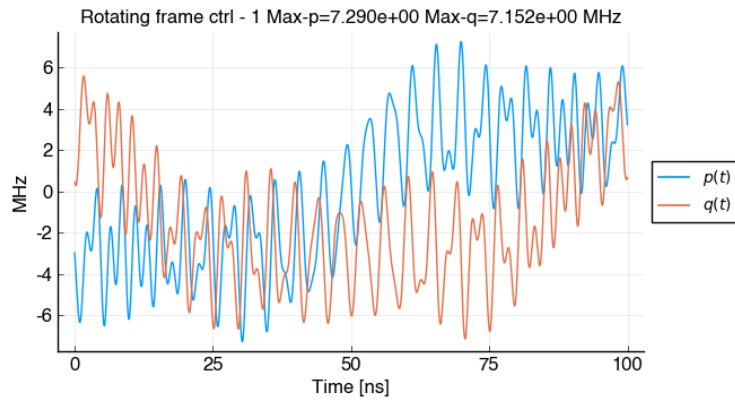


Figure 5: The rotating frame control functions  $p(t)$  (blue) and  $q(t)$  (orange) for realizing a CNOT gate with  $D_1 = 10$  basis function per carrier wave and three carrier wave frequencies. Here,  $\alpha_{max}/2\pi = 3$  MHz.

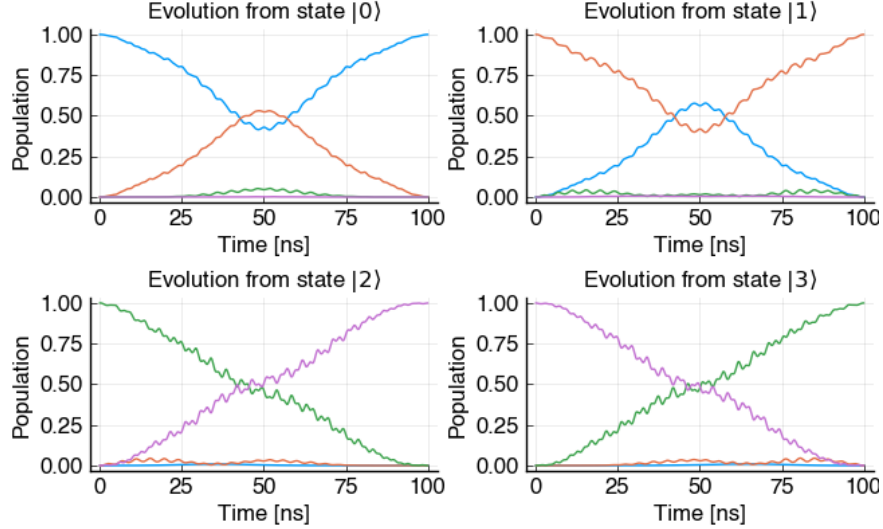


Figure 6: The population of the states  $|0\rangle$  (blue),  $|1\rangle$  (orange),  $|2\rangle$  (green) and  $|3\rangle$  (purple), as function of time, for each initial condition of the CNOT gate. Here,  $\alpha_{max}/2\pi = 3$  MHz.

corresponding to a trace fidelity greater than 0.9999. The population of the “forbidden” state  $|5\rangle$  has a population that remains below  $3.39 \cdot 10^{-7}$ .

### 6.2. The Hessian of the objective function

The numerical results shown in Figure 3 illustrate that the convergence properties of the optimization algorithm depend on the parameter constraints. To gain clarity into the local landscape of the optima we study the Hessian of the objective function. Let the optima correspond to the parameter vector  $\alpha^*$ . Based on the adjoint scheme for calculating the gradient, we can approximate the elements of the Hessian matrix using a centered finite difference approximation,

$$\frac{\partial^2 \mathcal{G}_h(\alpha^*)}{\partial \alpha_j \partial \alpha_k} \approx \frac{1}{2\varepsilon} \left( \frac{\partial \mathcal{G}_h}{\partial \alpha_j}(\alpha^* + \varepsilon e_k) - \frac{\partial \mathcal{G}_h}{\partial \alpha_j}(\alpha^* - \varepsilon e_k) \right) := L_{j,k}, \quad (61)$$

for  $j, k = 1, 2, \dots, D$ . To perform this calculation, the gradient must be evaluated for the  $2D$  parameter vectors  $(\alpha^* \pm \varepsilon e_k)$ . Because the objective function and the parameter vector are real-valued, the gradient and the Hessian are also real-valued. Due to the finite difference approximation, the matrix  $L$  is only approximately equal to the Hessian. The accuracy in  $L$  is estimated in Table 1 by studying the norm of its asymmetric part, which is zero for the Hessian. Based on this experiment we infer that  $\varepsilon = 10^{-6}$  is appropriate to use for approximating the Hessian in (61). To eliminate spurious effects from the asymmetry in the  $L$  matrix, we study the spectrum of its symmetric part,  $L_s = 0.5(L + L^T)$ . Because it is real and symmetric, it has a complete set of eigenvectors and all eigenvalues are real.

$\varepsilon$	$\ 0.5(L + L^T)\ _F$	$\ 0.5(L - L^T)\ _F$
$10^{-4}$	$4.95 \cdot 10^3$	$1.99 \cdot 10^{-4}$
$10^{-5}$	$4.95 \cdot 10^3$	$2.01 \cdot 10^{-6}$
$10^{-6}$	$4.95 \cdot 10^3$	$1.46 \cdot 10^{-6}$
$10^{-7}$	$4.95 \cdot 10^3$	$1.47 \cdot 10^{-5}$

Table 1: The Frobenius norm of the symmetric and asymmetric parts of the approximate Hessian,  $L$ , for the case  $\alpha_{max}/2\pi = 3.0$  MHz.

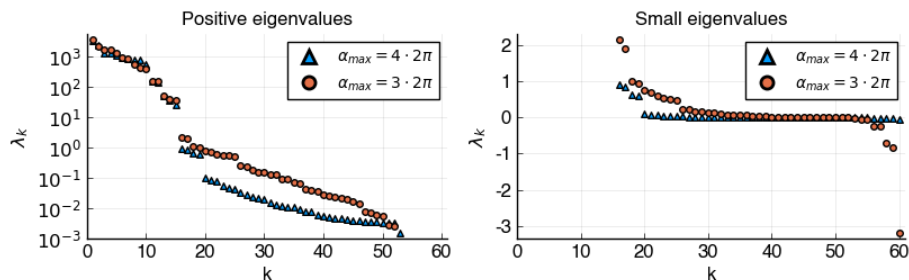


Figure 7: The eigenvalues of the symmetric part of the approximate Hessian,  $0.5(L + L^T)$ , evaluated at the optima for the parameter thresholds  $\alpha_{max}/2\pi = 4$  MHz (blue triangles) and  $\alpha_{max}/2\pi = 3$  MHz (orange circles). The positive eigenvalues are shown on a log-scale on the left and the small eigenvalues are shown on a linear scale on the right.

The eigenvalues of the Hessian are shown in Figure 7 for both values of the parameter threshold,  $\alpha_{max}$ . Two properties of the spectra are noteworthy. First, a few eigenvalues are negative. This may be an artifact related to the elements of the parameter vector that are close to their bounds. As a result the landscape of the objective function may not be accurately represented by the corresponding components of the Hessian. The second interesting property is that the 15 largest eigenvalues are significantly larger than the rest. This indicates that the control functions are essentially described by the 15 eigenvectors associated with those eigenvalues. As a result, the objective function varies much faster in those directions than in the directions of the remaining 45 eigenvectors and this may hamper the convergence of the optimization algorithm in that subspace. However, most of those 45 eigenvalues become larger when the parameter threshold is reduced from  $\alpha_{max}/2\pi = 4$  MHz to  $\alpha_{max}/2\pi = 3$  MHz. This indicates that the constraints on the parameter vector have a regularizing effect on the optimization problem and may explain why the latter case converges better (see Figure 3).

## 7. Comparing JuQBox with QuTiP/pulse\_optim and Grape-TF

The QuTiP/pulse\_optim package is part of the QuTiP [11] framework and implements the GRAPE algorithm in the Python language. The Grape-TF code

(TF is short for Tensorflow [1]) is also implemented in Python and provides an enhanced implementation of the GRAPE algorithm, as described by Leung et al. [13]. It is callable from QuTiP and shares a similar problem setup with the pulse\_optim function.

To compare the JuQBox code with pulse\_optim and Grape-TF, we consider a set of SWAP gates. These gates transform the ground state  $|0\rangle$  to excited state  $|d\rangle$ , and vice versa. The transformation can be described by the unitary matrix

$$V_g = \begin{bmatrix} 0 & 0 & \cdots & 0 & 1 \\ 0 & 1 & 0 & \cdots & 0 \\ \vdots & \ddots & \ddots & \ddots & \vdots \\ 0 & \cdots & 0 & 1 & 0 \\ 1 & 0 & \cdots & 0 & 0 \end{bmatrix} \in \mathbb{C}^{(d+1) \times (d+1)}, \quad (62)$$

which involves  $E = d + 1$  essential states. To evaluate how much leakage occurs to higher energy levels, we add one guard (forbidden) level ( $G = 1$ ) and evolve a total of  $N = d + 2$  states in Schrödinger's equation. As before, the guard level is left unspecified in the target gate transformation. We consider implementing the SWAP gates on a multi-level qudit that can be described by the fundamental frequency  $\omega_a/2\pi = 4.8$  GHz and the self-Kerr coefficient  $\xi_a/2\pi = 0.22$  GHz. We apply the rotating wave approximation, where the angular frequency of the rotation is  $\omega_a$ , resulting in the Hamiltonian model (4). As a realistic model for current superconducting quantum devices, we impose the control amplitude restrictions

$$\max_t |p(t, \boldsymbol{\alpha})| \leq c_\infty, \quad \max_t |q(t, \boldsymbol{\alpha})| \leq c_\infty, \quad \frac{c_\infty}{2\pi} = 9 \text{ MHz}, \quad (63)$$

in the rotating frame of reference.

### 7.1. Setup of simulation codes

QuTiP/pulse\_optim can minimize the target gate fidelity,  $\mathcal{G}_1$ , but does not suppress occupation of higher energy states. Thus, it does *not* minimize terms of the type  $\mathcal{G}_2$ . As a proxy for  $\mathcal{G}_2$ , we append one additional energy level to the simulation and measure its occupation as an estimate of leakage to higher energy states. In pulse\_optim, the control functions are discretized on the same grid in time as Schrödinger's equation and no smoothness conditions are imposed. In our tests, we use a random initial guess for the parameter vector.

Grape-TF discretizes the control functions on the same grid in time as Schrödinger's equation. It minimizes an objective function that consists of a number of user-configurable parts. In our test, we minimize the gate infidelity ( $\mathcal{G}_1$ ) and the occupation of one guard (forbidden) energy level (similar to  $\mathcal{G}_2$ ). To smooth the control functions in time, the objective function also contains additional terms to minimize their first and second time derivatives. The various

parts of the objective function are weighted together by user-specified coefficients. The gradient of the objective function is calculated using the automatic differentiation (AD) technique, as implemented in the Tensorflow package. In our tests, we use a random initial guess for the control vector.

In JuQBox, we trigger the first  $d$  transition frequencies in the Hamiltonian by using  $d$  carrier waves in the control functions, with angular frequencies

$$\Omega_k = (k - 1)(-\xi_a), \quad k = 1, 2, \dots, N_f, \quad N_f = d.$$

Similar to pulse\_optim and Grape-TF, a pseudo-random number generator is used to construct the initial guess for the parameter vector.

The pulse\_optim and JuQBox simulations were run on a Macbook Pro with a 2.6 GHz Intel iCore-7 processor. To utilize the GPU acceleration in Tensorflow, the Grape-TF simulations were run on one node of the Pascal machine at Livermore Computing, where each node has an Intel XEON E5-2695 v4 processor with two NVIDIA P-100 GPUs.

## 7.2. Numerical results

A SWAP gate where the control functions meet the control amplitude bounds (63) can only be realized if the gate duration is sufficiently long. Furthermore, the minimum gate duration increases with  $d$ . For each value of  $d$ , we used numerical experiments to determine a duration  $T_d$  such that at least two of the three simulation codes could find a solution with a small gate infidelity. For JuQBox, we used the technique in Section 3.2 with  $C_P = 80$  to obtain the number of time steps. The number of control parameters follow from  $D = 2N_f D_1$ , where  $N_f = d$  equals the number of carrier wave frequencies and  $D_1$  is the number of B-splines per control functions. Here,  $D_1 = 10$  for  $d = 3, 4, 5$  and  $D_1 = 20$  for  $d = 6$ . For pulse\_optim and Grape-TF, we calculate the number of time steps based on the shortest transition period, corresponding to the highest transition frequency in the system. We then use 40 time steps per shortest transition period to resolve the control functions. For both GRAPE methods there are 2 control parameters per time step. The main simulation parameters are given in Table 2.

Optimization results for the pulse\_optim, Grape-TF and JuQBox codes are presented in Tables 3, 4 and 5. The pulse\_optim code generates piecewise constant control functions that are very noisy and may therefore be hard to realize experimentally. To obtain a realistic estimate of the resulting dynamics, we interpolate the optimized control functions on a grid with 20 times smaller time step and use the `mesolve()` function in QuTiP to calculate the evolution of the system from each initial state. We then evaluate the gate infidelity using the evolved states at the final time, denoted by  $\mathcal{G}_1^*$  in Table 3. Since the control functions from Grape-TF and JuQBox are significantly smoother, we report the target gate fidelities as calculated by those codes.

For the  $|0\rangle \leftrightarrow |3\rangle$ ,  $|0\rangle \leftrightarrow |4\rangle$  and  $|0\rangle \leftrightarrow |5\rangle$  SWAP gates, all three codes produce control functions with very small gate infidelities. We note that the population of the guard level,  $|\psi^{(d+1)}|^2$ , is about an order of magnitude larger

		# time steps		# parameters	
$d$	$T_d$ [ns]	JuQBox	GRAPE	JuQBox	GRAPE
3	140	14,787	4,480	60	8,960
4	215	37,843	7,568	80	15,136
5	265	69,962	11,661	100	23,322
6	425	157,082	22,441	240	44,882

Table 2: Gate duration, number of time steps ( $M$ ) and total number of control parameters ( $D$ ) in the  $|0\rangle \leftrightarrow |d\rangle$  SWAP gate simulations. The number of time steps and control parameters are the same for pulse\_optim and Grape-TF.

$d$	$\mathcal{G}_1^*$	$ \psi^{(d+1)} _\infty^2$	$ p _\infty$ [MHz]	$ q _\infty$ [MHz]	# iter	CPU [s]
3	4.35e-6	9.41e-3	9.00	9.00	38	30
4	3.91e-5	1.20e-2	9.00	9.00	93	108
5	1.57e-4	8.77e-3	9.00	9.00	215	385
6	<b>1.76e-3</b>	<b>4.48e-2</b>	9.00	9.00	246	894

Table 3: QuTiP/pulse\_optim results for  $|0\rangle \leftrightarrow |d\rangle$  SWAP gates. Note the larger infidelity and guard state population for  $d = 6$ .

$d$	$\mathcal{G}_1$	$ \psi^{(d+1)} _\infty^2$	$ p _\infty$ [MHz]	$ q _\infty$ [MHz]	# iter	CPU [s]
3	8.76e-6	4.03e-3	6.98	8.83	78	2,062
4	1.52e-5	3.39e-3	6.87	6.54	128	10,601
5	2.80e-5	1.78e-3	7.21	7.62	161	28,366
6	<b>4.89e-1</b>	2.33e-5	0.73	0.74	93	81,765

Table 4: Grape-TF results for  $|0\rangle \leftrightarrow |d\rangle$  SWAP gates. Note the very large infidelity for  $d = 6$ . These simulations used two NVIDIA P-100 GPUs to accelerate Tensorflow.

$d$	$\mathcal{G}_1$	$ \psi^{(d+1)} _\infty^2$	$ p _\infty$ [MHz]	$ q _\infty$ [MHz]	# iter	CPU
3	2.71e-5	1.92e-3	7.59	8.99	177	55
4	4.91e-5	1.23e-3	7.78	5.33	166	151
5	4.95e-5	1.25e-3	7.42	7.24	173	291
6	7.41e-6	4.41e-3	4.55	5.39	229	1255

Table 5: JuQBox results for  $|0\rangle \leftrightarrow |d\rangle$  SWAP gates.

with pulse\_optim than with JuQBox; the guard level population from Grape-TF are somewhere in between. The most significant difference between the results occur for the  $d = 6$  SWAP gate. Here, the Grape-TF code fails to produce a small gate infidelity after running for almost 23 hours and the pulse\_optim code results in a gate fidelity that is about 2 orders of magnitude larger than JuQBox.

While pulse\_optim and JuQBox require comparable amounts of CPU time to converge, the Grape-TF code is between 50-100 times slower, despite the GPU acceleration.

We proceed by analyzing the optimized control functions and take the  $|0\rangle \leftrightarrow |5\rangle$  SWAP gate as a representative example. In this case, the relevant transition frequencies in the laboratory frame of reference are

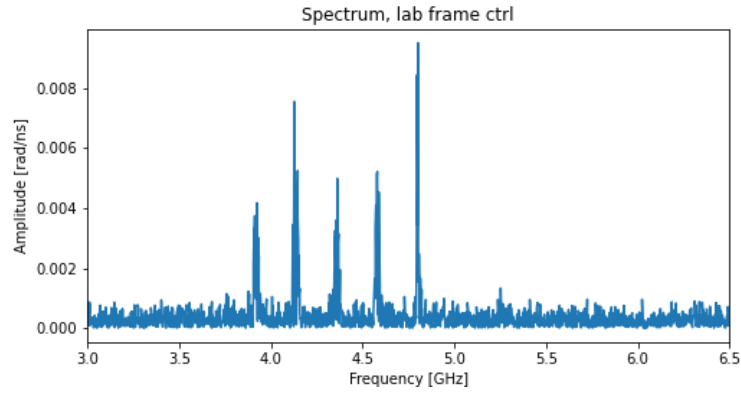
$$f_k = \frac{1}{2\pi} (\omega_a - k\xi_a), \quad k = 0, 1, 2, 3, 4. \quad (64)$$

To compare the optimized control functions, we evaluate the corresponding laboratory frame control function using (5) and study its Fourier spectrum. Results from the pulse\_optim, Grape-TF and JuQBox simulations are presented in Figure 8. We first note that pulse\_optim produces a significantly noisier control function compared to the other two codes. The control function from Grape-TF is significantly smoother, even though its spectrum includes some noticeable peaks at frequencies that do not correspond to transition frequencies in the system. The JuQBox simulation results in a laboratory frame control function where each peak in the spectrum corresponds to a transition frequency in the Hamiltonian.

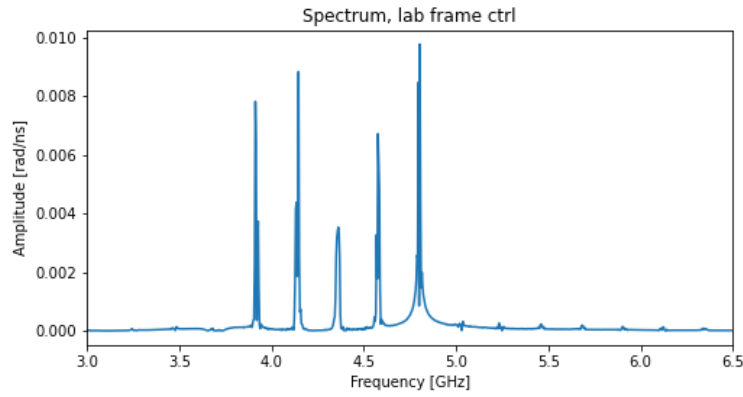
## 8. Conclusions

In this paper we have developed numerical methods for optimizing control functions for realizing logical gates in a closed quantum system. The quantum state is governed by Schrödinger's equation, which is a time-dependent Hamiltonian system. To ensure long-time numerical accuracy we discretize it using the symplectic Störmer-Verlet method, which can be written as a partitioned Runge-Kutta scheme. Our main theoretical contribution is the derivation of a compatible time-discretization of the adjoint state equation, such that the gradient of the discrete objective function can be calculated exactly. This scheme generalizes Ober-Blöbaum's [18] methods to the case of a time-dependent Hamiltonian system.

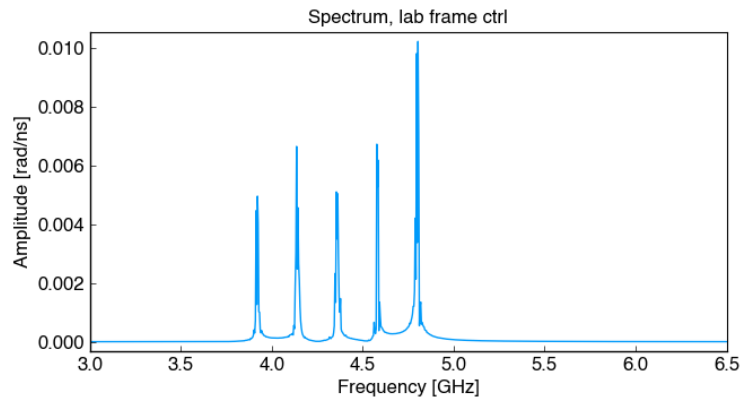
We have also introduced a parameterization of the control functions based on B-splines with built-in carrier waves. The carrier waves are used to specify the frequency spectra of the control functions, while the B-spline functions specify their envelope and phase. This approach allows the number of control parameters to be independent of, and significantly smaller than, the number of time steps for integrating Schrödinger's equation. Our numerical solution of the optimal control problem is based on the general purpose interior-point optimization package IPOPT [21], which implements a primal-dual barrier approach



(a) QuTiP/pulse\_optim.



(b) Grape-TF.



(c) JuQBox.

Figure 8: Magnitude of the Fourier spectrum of the laboratory frame control function for the  $|0\rangle \leftrightarrow |5\rangle$  SWAP gate.

for minimizing the objective function subject to amplitude constraints on the parameter vector. We optimized the control functions for a CNOT gate with two guard states, resulting in a gate trace fidelity greater than 0.9999. Having a moderate number of control parameters enabled us to study the spectrum of the Hessian of the objective function at an optima. We found that imposing tighter bounds on the parameter vector results in a Hessian with larger eigenvalues and thus improves the convergence of the optimization algorithm.

The performance of the proposed algorithm, implemented in a code called JuQBox, was compared with two implementations of the GRAPE algorithm: QuTiP/pulse.optim [11] and Grape-Tensorflow [13]. JuQBox was found to produce significantly smoother control functions than QuTiP/pulse.optim, while using about the same computational resources. JuQBox was also found to run about 50-100 times faster than Grape-Tensorflow.

In future work, it would be interesting to study if the convergence properties of the optimization algorithm can be improved by modifying the objective function. We also intend to generalize our approach to solve optimal control problem for open quantum systems.

## Acknowledgment

We would like to thank Prof. Daniel Appelö for bringing the Störmer-Verlet method to our attention.

This work was supported in part by LLNL laboratory directed research and development project 20-ERD-028 and in part by DOE office of advanced scientific computing research (OASCR) under the Advanced Research in Quantum Computing (ARQC) program, award 2019-LLNL-SCW-1683.

This work performed under the auspices of the U.S. Department of Energy by Lawrence Livermore National Laboratory under Contract DE-AC52-07NA27344. This is contribution LLNL-JRNL-800457.

## Appendix A. The Hamiltonian in a rotating frame of reference

In the laboratory frame of reference, the Hamiltonian matrix for a single superconducting qudit can be modeled by

$$H(t) = \omega_a a^\dagger a - \frac{\xi_a}{2} a^\dagger a^\dagger a a + f(t)(a + a^\dagger). \quad (\text{A.1})$$

Here,  $\omega_a > 0$  and  $\xi_a$  are given real constants and  $f(t, \boldsymbol{\alpha})$  is a real-valued function of time that depend on the parameter vector  $\boldsymbol{\alpha}$ . Furthermore,  $a$  is the lowering matrix,

$$a = \begin{bmatrix} 0 & 1 & & & & \\ & 0 & \sqrt{2} & & & \\ & & \ddots & \ddots & & \\ & & & 0 & \sqrt{N-1} & \\ & & & & & 0 \end{bmatrix},$$

and the raising matrix  $a^\dagger$  is its adjoint (conjugate transpose).

To derive the rotating frame transformation, we consider the time-dependent change of variable

$$\psi(t) = R^\dagger(t)\tilde{\psi}(t), \quad R^\dagger R = I.$$

We have

$$\dot{\psi} = \dot{R}^\dagger \tilde{\psi} + R^\dagger \dot{\tilde{\psi}}, \quad H\psi = HR^\dagger \tilde{\psi}.$$

After some algebra, the Schrödinger equation (7) and the identity  $R\dot{R}^\dagger = -\dot{R}R^\dagger$  gives:

$$\dot{\tilde{\psi}} = -i\tilde{H}(t)\tilde{\psi}, \quad \tilde{H}(t) = R(t)H(t)R(t)^\dagger + i\dot{R}(t)R(t)^\dagger. \quad (\text{A.2})$$

The rotating frame of reference is introduced by taking the unitary transformation to be

$$R(t) = \exp(i\omega_a t a^\dagger a), \quad a^\dagger a = \begin{bmatrix} 0 & & & & \\ & 1 & & & \\ & & 2 & & \\ & & & \ddots & \\ & & & & N-1 \end{bmatrix}, \quad \dot{R}R^\dagger = i\omega_a a^\dagger a. \quad (\text{A.3})$$

From (A.2) and (A.3), the first term in the Hamiltonian (A.1) is canceled by the term  $i\dot{R}(t)R(t)^\dagger$ . Furthermore,  $a^\dagger a^\dagger a a = (a^\dagger a)^2 - a^\dagger a$  and both  $a^\dagger a$  and  $(a^\dagger a)^2$  commute with  $R(t)$ . After noting that  $R a^\dagger R^\dagger = e^{i\omega_a t} a^\dagger$ , the transformed Hamiltonian can be written

$$\tilde{H}(t) = -\frac{\xi_a}{2} ((a^\dagger a)^2 - a^\dagger a) + f(t) (e^{-i\omega_a t} a + e^{i\omega_a t} a^\dagger). \quad (\text{A.4})$$

To slow down the time scales in the control function, we want to absorb the highly oscillatory factors  $\exp(\pm i\omega_a t)$  into  $f(t)$ . Because the control function  $f(t)$  is real-valued, this can only be done in an approximate fashion. We make the ansatz,

$$f(t) = 2p(t) \cos(\omega_a t) - 2q(t) \sin(\omega_a t) = (p + iq) \exp(i\omega_a t) + (p - iq) \exp(-i\omega_a t), \quad (\text{A.5})$$

where  $p(t)$  and  $q(t)$  are real-valued functions. After some algebra, the transformed Hamiltonian (A.4) becomes

$$\begin{aligned} \tilde{H}(t) = & -\frac{\xi_a}{2} ((a^\dagger a)^2 - a^\dagger a) + p(a + a^\dagger) + iq(a - a^\dagger) \\ & + (p - iq) \exp(-2i\omega_a t) a + (p + iq) \exp(2i\omega_a t) a^\dagger. \end{aligned}$$

The rotating frame approximation follows by ignoring the terms that oscillate with twice the frequency,  $\exp(\pm 2i\omega_a t)$ , resulting in the transformed Schrödinger

system,

$$\dot{\tilde{\psi}}_j = -i \left( H_d + \tilde{H}_c(t) \right) \tilde{\psi}_j, \quad \tilde{\psi}_j(0) = \mathbf{e}_j, \quad (\text{A.6})$$

$$H_d = -\frac{\xi_a}{2} (a^\dagger a^\dagger a a), \quad \tilde{H}_c(t) = p(t) (a + a^\dagger) + iq(t) (a - a^\dagger). \quad (\text{A.7})$$

Here,  $H_d$  is called the drift Hamiltonian. When  $\xi_a \ll \omega_a$ , the state vector varies on a significantly slower time scale in the rotating frame than in the laboratory frame.

In the remainder of the paper, the Schrödinger equation is always solved under the rotating frame approximation and we drop the tildes on the state vector and the Hamiltonian matrices.

## Appendix B. Derivation of the discrete adjoint scheme

We seek to determine a scheme for evolving the Lagrange multiplier (adjoint) variables to satisfy the first order optimality conditions (42). In the following, let  $\delta_{r,s}$  denote the usual Kronecker delta function.

The terms  $T_j^3$  to  $T_j^6$  in (38) enforce the relations between the stage variables (30)-(33) according to

$$T_j^3 = \sum_{n=0}^{M-1} \left\langle \mathbf{U}_j^{n,1} - \mathbf{u}_j^n, \mathbf{M}_j^{n,1} \right\rangle_2, \quad (\text{B.1})$$

$$T_j^4 = \sum_{n=0}^{M-1} \left\langle \mathbf{U}_j^{n,2} - \mathbf{u}_j^n - \frac{h}{2} \left( S_n \mathbf{U}_j^{n,1} + S_{n+1} \mathbf{U}_j^{n,2} - K_n \mathbf{V}_j^{n,1} - K_{n+1} \mathbf{V}_j^{n,2} \right), \mathbf{M}_j^{n,2} \right\rangle_2, \quad (\text{B.2})$$

$$T_j^5 = \sum_{n=0}^{M-1} \left\langle \mathbf{V}_j^{n,1} - \mathbf{v}_j^n - \frac{h}{2} \left( K_{n+1/2} \mathbf{U}_j^{n,1} + S_{n+1/2} \mathbf{V}_j^{n,1} \right), \mathbf{N}_j^{n,1} \right\rangle_2, \quad (\text{B.3})$$

$$T_j^6 = \sum_{n=0}^{M-1} \left\langle \mathbf{V}_j^{n,2} - \mathbf{v}_j^n - \frac{h}{2} \left( K_{n+1/2} \mathbf{U}_j^{n,1} + S_{n+1/2} \mathbf{V}_j^{n,1} \right), \mathbf{N}_j^{n,2} \right\rangle_2. \quad (\text{B.4})$$

Taking the derivative of (38) with respect to  $\mathbf{u}_j^r$

$$0 = \frac{\partial \mathcal{L}_h}{\partial \mathbf{u}_j^r} = \frac{\partial \mathcal{J}_h}{\partial \mathbf{u}_j^r} - \left[ (\boldsymbol{\mu}_j^n - \boldsymbol{\mu}_j^{n+1}) \delta_{r,n} + \boldsymbol{\mu}_j^M \delta_{r,M} - (\mathbf{M}_j^{n,1} + \mathbf{M}_j^{n,2}) \delta_{r,n} \right],$$

which gives the conditions

$$\boldsymbol{\mu}_j^M = \frac{\partial \mathcal{J}_h}{\partial \mathbf{u}_j^M}, \quad \boldsymbol{\mu}_j^n - \boldsymbol{\mu}_j^{n+1} = \mathbf{M}_j^{n,1} + \mathbf{M}_j^{n,2}, \quad n = 0, 1, \dots, M-1.$$

Similarly, differentiating (38) with respect to  $\mathbf{v}_j^r$  gives

$$0 = \frac{\partial \mathcal{L}_h}{\partial \mathbf{v}_j^r} = \frac{\partial \mathcal{J}_h}{\partial \mathbf{v}_j^r} - \left[ (\boldsymbol{\nu}_j^n - \boldsymbol{\nu}_j^{n+1}) \delta_{r,n} + \boldsymbol{\nu}_j^M \delta_{r,M} - (\mathbf{N}_j^{n,1} + \mathbf{N}_j^{n,2}) \delta_{r,n} \right],$$

which leads to the conditions

$$\boldsymbol{\nu}_j^n - \boldsymbol{\nu}_j^{n+1} = \mathbf{N}_j^{n,1} + \mathbf{N}_j^{n,2}, \quad \boldsymbol{\nu}_j^M = \frac{\partial \mathcal{J}_h}{\partial \mathbf{v}_j^M}.$$

Next we take the derivative of (38) with respect to  $\mathbf{U}_j^{n,1}$ ,

$$\begin{aligned} \frac{\partial \mathcal{L}_h}{\partial \mathbf{U}_j^{n,1}} &= \frac{\partial \mathcal{J}_h}{\partial \mathbf{U}_j^{n,1}} - \sum_{i=1}^6 \frac{\partial T_j^i}{\partial \mathbf{U}_j^{n,1}} = 0, \\ \frac{\partial T_j^1}{\partial \mathbf{U}_j^{n,1}} &= -\frac{h}{2} S_n^T \boldsymbol{\mu}_j^{n+1}, \\ \frac{\partial T_j^2}{\partial \mathbf{U}_j^{n,1}} &= -\frac{h}{2} K_{n+1/2}^T \boldsymbol{\nu}_j^{n+1}, \\ \frac{\partial T_j^3}{\partial \mathbf{U}_j^{n,1}} &= \mathbf{M}_j^{n,1}, \\ \frac{\partial T_j^4}{\partial \mathbf{U}_j^{n,1}} &= -\frac{h}{2} S_n^T \mathbf{M}_j^{n,2}, \\ \frac{\partial T_j^5}{\partial \mathbf{U}_j^{n,1}} &= -\frac{h}{2} K_{n+1/2}^T \mathbf{N}_j^{n,1}, \\ \frac{\partial T_j^6}{\partial \mathbf{U}_j^{n,1}} &= -\frac{h}{2} K_{n+1/2}^T \mathbf{N}_j^{n,2}, \end{aligned}$$

which, using the fact that  $S_n^T = -S_n$  and  $K_n^T = K_n$ , we may write as

$$\mathbf{M}_j^{n,1} + \frac{h}{2} S_n \left( \boldsymbol{\mu}_j^{n+1} + \mathbf{M}_j^{n,2} \right) - \frac{h}{2} K_{n+1/2} \left( \boldsymbol{\nu}_j^{n+1} + \mathbf{N}_j^{n,1} + \mathbf{N}_j^{n,2} \right) = \frac{\partial \mathcal{J}_h}{\partial \mathbf{U}_j^{n,1}}.$$

Repeating this procedure for the derivative with respect to  $\mathbf{U}_j^{n,2}$  gives

$$\begin{aligned} \frac{\partial \mathcal{L}_h}{\partial \mathbf{U}_j^{n,2}} &= \frac{\partial \mathcal{J}_h}{\partial \mathbf{U}_j^{n,2}} - \sum_{i=1}^6 \frac{\partial T_j^i}{\partial \mathbf{U}_j^{n,2}} = 0, \\ \frac{\partial T_j^1}{\partial \mathbf{U}_j^{n,2}} &= -\frac{h}{2} S_{n+1}^T \boldsymbol{\mu}_j^{n+1}, \\ \frac{\partial T_j^2}{\partial \mathbf{U}_j^{n,2}} &= -\frac{h}{2} K_{n+1/2}^T \boldsymbol{\nu}_j^{n+1}, \\ \frac{\partial T_j^4}{\partial \mathbf{U}_j^{n,2}} &= \mathbf{M}_j^{n,2} - \frac{h}{2} S_{n+1}^T \mathbf{M}_j^{n,2}, \\ \frac{\partial T_j^3}{\partial \mathbf{U}_j^{n,2}} &= \frac{\partial T_j^5}{\partial \mathbf{U}_j^{n,2}} = \frac{\partial T_j^6}{\partial \mathbf{U}_j^{n,2}} = 0, \end{aligned}$$

which we may write compactly as

$$\mathbf{M}_j^{n,2} + \frac{h}{2} S_{n+1} \left( \boldsymbol{\mu}_j^{n+1} + \mathbf{M}_j^{n,2} \right) - \frac{h}{2} K_{n+1/2} \boldsymbol{\nu}_j^{n+1} = \frac{\partial \mathcal{J}_h}{\partial \mathbf{U}_j^{n,2}}.$$

Taking the derivative of (38) with respect to  $\mathbf{V}_j^{n,1}$  gives the set of equations

$$\begin{aligned} \frac{\partial \mathcal{L}_h}{\partial \mathbf{V}_j^{n,1}} &= \frac{\partial \mathcal{J}_h}{\partial \mathbf{V}_j^{n,1}} - \sum_{i=1}^6 \frac{\partial T_j^i}{\partial \mathbf{V}_j^{n,1}} = 0, \\ \frac{\partial T_j^1}{\partial \mathbf{V}_j^{n,1}} &= \frac{h}{2} K_n^T \boldsymbol{\mu}_j^{n+1}, \\ \frac{\partial T_j^2}{\partial \mathbf{V}_j^{n,1}} &= -\frac{h}{2} S_{n+1/2}^T \boldsymbol{\nu}_j^{n+1}, \\ \frac{\partial T_j^3}{\partial \mathbf{V}_j^{n,1}} &= 0, \\ \frac{\partial T_j^4}{\partial \mathbf{V}_j^{n,1}} &= \frac{h}{2} K_n^T \mathbf{M}_j^{n,2}, \\ \frac{\partial T_j^5}{\partial \mathbf{V}_j^{n,1}} &= \mathbf{N}_j^{n,1} - \frac{h}{2} S_{n+1/2}^T \mathbf{N}_j^{n,1}, \\ \frac{\partial T_j^6}{\partial \mathbf{V}_j^{n,1}} &= -\frac{h}{2} S_{n+1/2}^T \mathbf{N}_j^{n,2}, \end{aligned}$$

which gives the condition

$$\mathbf{N}_j^{n,1} + \frac{h}{2} S_{n+1/2} \left( \boldsymbol{\nu}_j^{n+1} + \mathbf{N}_j^{n,1} + \mathbf{N}_j^{n,2} \right) + \frac{h}{2} K_n \left( \boldsymbol{\mu}_j^{n+1} + \mathbf{M}_j^{n,2} \right) = \frac{\partial \mathcal{J}_h}{\partial \mathbf{V}_j^{n,1}}.$$

Similarly, taking the derivative with respect to  $\mathbf{V}_j^{n,2}$  gives

$$\begin{aligned}\frac{\partial \mathcal{L}_h}{\partial \mathbf{V}_j^{n,2}} &= \frac{\partial \mathcal{J}_h}{\partial \mathbf{V}_j^{n,2}} - \sum_{i=1}^6 \frac{\partial T_j^i}{\partial \mathbf{V}_j^{n,2}} = 0, \\ \frac{\partial T_j^1}{\partial \mathbf{V}_j^{n,2}} &= \frac{h}{2} K_{n+1}^T \boldsymbol{\mu}_j^{n+1}, \\ \frac{\partial T_j^2}{\partial \mathbf{V}_j^{n,2}} &= -\frac{h}{2} S_{n+1/2}^T \boldsymbol{\nu}_j^{n+1}, \\ \frac{\partial T_j^4}{\partial \mathbf{V}_j^{n,2}} &= \frac{h}{2} K_{n+1}^T \mathbf{M}_j^{n,2}, \\ \frac{\partial T_j^6}{\partial \mathbf{V}_j^{n,2}} &= \mathbf{N}_j^{n,2}, \\ \frac{\partial T_j^3}{\partial \mathbf{V}_j^{n,2}} &= \frac{\partial T_j^5}{\partial \mathbf{V}_j^{n,2}} = 0,\end{aligned}$$

giving

$$\mathbf{N}_j^{n,2} + \frac{h}{2} S_{n+1/2} \boldsymbol{\nu}_j^{n+1} + \frac{h}{2} K_{n+1} \left( \boldsymbol{\mu}_j^{n+1} + \mathbf{M}_j^{n,2} \right) = \frac{\partial \mathcal{J}_h}{\partial \mathbf{V}_j^{n,2}}.$$

In summary, the first order optimality conditions (42) are satisfied if the following equations hold:

$$\boldsymbol{\mu}_j^n - \boldsymbol{\mu}_j^{n+1} = \mathbf{M}_j^{n,1} + \mathbf{M}_j^{n,2}, \quad \boldsymbol{\mu}_j^M = \frac{\partial \mathcal{J}_h}{\partial \mathbf{u}_j^M}, \quad (\text{B.5})$$

$$\boldsymbol{\nu}_j^n - \boldsymbol{\nu}_j^{n+1} = \mathbf{N}_j^{n,1} + \mathbf{N}_j^{n,2}, \quad \boldsymbol{\nu}_j^M = \frac{\partial \mathcal{J}_h}{\partial \mathbf{v}_j^M}, \quad (\text{B.6})$$

$$\mathbf{M}_j^{n,1} + \frac{h}{2} S_n \left( \boldsymbol{\mu}_j^{n+1} + \mathbf{M}_j^{n,2} \right) - \frac{h}{2} K_{n+1/2} \left( \boldsymbol{\nu}_j^{n+1} + \mathbf{N}_j^{n,1} + \mathbf{N}_j^{n,2} \right) = \frac{\partial \mathcal{J}_h}{\partial \mathbf{U}_j^{n,1}}, \quad (\text{B.7})$$

$$\mathbf{M}_j^{n,2} + \frac{h}{2} S_{n+1} \left( \boldsymbol{\mu}_j^{n+1} + \mathbf{M}_j^{n,2} \right) - \frac{h}{2} K_{n+1/2} \boldsymbol{\nu}_j^{n+1} = \frac{\partial \mathcal{J}_h}{\partial \mathbf{U}_j^{n,2}}, \quad (\text{B.8})$$

$$\mathbf{N}_j^{n,1} + \frac{h}{2} S_{n+1/2} \left( \boldsymbol{\nu}_j^{n+1} + \mathbf{N}_j^{n,1} + \mathbf{N}_j^{n,2} \right) + \frac{h}{2} K_n \left( \boldsymbol{\mu}_j^{n+1} + \mathbf{M}_j^{n,2} \right) = \frac{\partial \mathcal{J}_h}{\partial \mathbf{V}_j^{n,1}}, \quad (\text{B.9})$$

$$\mathbf{N}_j^{n,2} + \frac{h}{2} S_{n+1/2} \boldsymbol{\nu}_j^{n+1} + \frac{h}{2} K_{n+1} \left( \boldsymbol{\mu}_j^{n+1} + \mathbf{M}_j^{n,2} \right) = \frac{\partial \mathcal{J}_h}{\partial \mathbf{V}_j^{n,2}}. \quad (\text{B.10})$$

We now consider the following change of variables

$$\mathbf{X}_j^n = \boldsymbol{\mu}_j^{n+1} + \mathbf{M}_j^{n,2}, \quad (\text{B.11})$$

$$\mathbf{Y}_j^{n,1} = \boldsymbol{\nu}_j^{n+1} + \mathbf{N}_j^{n,1} + \mathbf{N}_j^{n,2}, \quad (\text{B.12})$$

$$\mathbf{Y}_j^{n,2} = \boldsymbol{\nu}_j^{n+1}, \quad (\text{B.13})$$

which, upon substitution into (B.7)-(B.10), gives the set of equations

$$\mathbf{M}_j^{n,1} + \frac{h}{2} S_n \mathbf{X}_j^n - \frac{h}{2} K_{n+1/2} \mathbf{Y}_j^{n,1} = \frac{\partial \mathcal{J}_h}{\partial \mathbf{U}_j^{n,1}}, \quad (\text{B.14})$$

$$\mathbf{M}_j^{n,2} + \frac{h}{2} S_{n+1} \mathbf{X}_j^n - \frac{h}{2} K_{n+1/2} \mathbf{Y}_j^{n,2} = \frac{\partial \mathcal{J}_h}{\partial \mathbf{U}_j^{n,2}}, \quad (\text{B.15})$$

$$\mathbf{N}_j^{n,1} + \frac{h}{2} S_{n+1/2} \mathbf{Y}_j^{n,1} + \frac{h}{2} K_n \mathbf{X}_j^n = \frac{\partial \mathcal{J}_h}{\partial \mathbf{V}_j^{n,1}}, \quad (\text{B.16})$$

$$\mathbf{N}_j^{n,2} + \frac{h}{2} S_{n+1/2} \mathbf{Y}_j^{n,2} + \frac{h}{2} K_{n+1} \mathbf{X}_j^n = \frac{\partial \mathcal{J}_h}{\partial \mathbf{V}_j^{n,2}}. \quad (\text{B.17})$$

By adding (B.14)-(B.15),

$$\mathbf{M}_j^{n,1} + \mathbf{M}_j^{n,2} = -\frac{h}{2} \left[ (S_n + S_{n+1}) \mathbf{X}_j^n - K_{n+1/2} (\mathbf{Y}_j^{n,1} + \mathbf{Y}_j^{n,2}) \right] + \frac{\partial \mathcal{J}_h}{\partial \mathbf{U}_j^{n,1}} + \frac{\partial \mathcal{J}_h}{\partial \mathbf{U}_j^{n,2}}. \quad (\text{B.18})$$

Similarly, by adding (B.16)-(B.17),

$$\mathbf{N}_j^{n,1} + \mathbf{N}_j^{n,2} = -\frac{h}{2} \left[ S_{n+1/2} (\mathbf{Y}_j^{n,1} + \mathbf{Y}_j^{n,2}) + (K_n + K_{n+1}) \mathbf{X}_j^n \right] + \frac{\partial \mathcal{J}_h}{\partial \mathbf{V}_j^{n,1}} + \frac{\partial \mathcal{J}_h}{\partial \mathbf{V}_j^{n,2}}. \quad (\text{B.19})$$

Thus, (B.5)-(B.6) can be rewritten as

$$\boldsymbol{\mu}_j^n - \boldsymbol{\mu}_j^{n+1} = -\frac{h}{2} \left[ (S_n + S_{n+1}) \mathbf{X}_j^n - K_{n+1/2} (\mathbf{Y}_j^{n,1} + \mathbf{Y}_j^{n,2}) \right] + \frac{\partial \mathcal{J}_h}{\partial \mathbf{U}_j^{n,1}} + \frac{\partial \mathcal{J}_h}{\partial \mathbf{U}_j^{n,2}} \quad (\text{B.20})$$

$$\boldsymbol{\nu}_j^n - \boldsymbol{\nu}_j^{n+1} = -\frac{h}{2} \left[ S_{n+1/2} (\mathbf{Y}_j^{n,1} + \mathbf{Y}_j^{n,2}) + (K_n + K_{n+1}) \mathbf{X}_j^n \right] + \frac{\partial \mathcal{J}_h}{\partial \mathbf{V}_j^{n,1}} + \frac{\partial \mathcal{J}_h}{\partial \mathbf{V}_j^{n,2}} \quad (\text{B.21})$$

By combining  $\mathbf{X}_j^n = \boldsymbol{\mu}_j^{n+1} + \mathbf{M}_j^{n,2}$  and (B.15),

$$\mathbf{X}_j^n = \boldsymbol{\mu}_j^{n+1} - \frac{h}{2} S_{n+1} \mathbf{X}_j^n + \frac{h}{2} K_{n+1/2} \mathbf{Y}_j^{n,2} + \frac{\partial \mathcal{J}_h}{\partial \mathbf{U}_j^{n,2}}. \quad (\text{B.22})$$

Similarly, by combining  $\mathbf{Y}_j^{n,1} = \boldsymbol{\nu}_j^{n+1} + \mathbf{N}_j^{n,1} + \mathbf{N}_j^{n,2}$  and (B.19),

$$\mathbf{Y}_j^{n,1} = \boldsymbol{\nu}_j^{n+1} - \frac{h}{2} \left[ S_{n+1/2} \left( \mathbf{Y}_j^{n,1} + \mathbf{Y}_j^{n,2} \right) + (K_n + K_{n+1}) \mathbf{X}_j^n \right] + \frac{\partial \mathcal{J}_h}{\partial \mathbf{V}_j^{n,1}} + \frac{\partial \mathcal{J}_h}{\partial \mathbf{V}_j^{n,2}}. \quad (\text{B.23})$$

The time-stepping scheme is completed by the relation

$$\mathbf{Y}^{n,2} = \boldsymbol{\nu}_j^{n+1}. \quad (\text{B.24})$$

The scheme (B.20)-(B.24) may be written in the form of Lemma 1 by defining the slopes according to (46)-(49). This completes the proof of the lemma.

### Appendix C. Proof of Corollary 1

By rearranging (44) and (45),

$$\boldsymbol{\mu}_j^{n+1} = \boldsymbol{\mu}_j^n + \frac{h}{2} \left( \boldsymbol{\kappa}_j^{n,1} + \boldsymbol{\kappa}_j^{n,2} \right), \quad (\text{C.1})$$

$$\boldsymbol{\nu}_j^{n+1} = \boldsymbol{\nu}_j^n + \frac{h}{2} \left( \boldsymbol{\ell}_j^{n,1} + \boldsymbol{\ell}_j^{n,2} \right). \quad (\text{C.2})$$

Hence,  $b_1^\mu = b_2^\mu = 1/2$  and  $b_1^\nu = b_2^\nu = 1/2$ .

To express the stage variables in standard form we substitute (C.1) into (50) and define  $\mathbf{X}_j^{n,1} = \mathbf{X}_j^{n,2} = \mathbf{X}_j^n$ . Similarly, we substitute (C.2) into (51) and (52), resulting in

$$\begin{aligned} \mathbf{X}_j^{n,1} &= \boldsymbol{\mu}_j^n + \frac{h}{2} \boldsymbol{\kappa}_j^{n,1}, \\ \mathbf{X}_j^{n,2} &= \boldsymbol{\mu}_j^n + \frac{h}{2} \boldsymbol{\kappa}_j^{n,1}, \\ \mathbf{Y}_j^{n,1} &= \boldsymbol{\nu}_j^n, \\ \mathbf{Y}_j^{n,2} &= \boldsymbol{\nu}_j^n + \frac{h}{2} \left( \boldsymbol{\ell}_j^{n,1} + \boldsymbol{\ell}_j^{n,2} \right). \end{aligned}$$

From these relations we can identify  $a_{11}^\mu = a_{21}^\mu = 1/2$  and  $a_{12}^\mu = a_{22}^\mu = 0$ . Furthermore,  $a_{11}^\nu = a_{12}^\nu = 0$  and  $a_{21}^\nu = a_{22}^\nu = 1/2$ .

For the case without forcing, the formulae for the slopes, (50)-(52), become

$$\boldsymbol{\kappa}_j^{n,1} = S_n \mathbf{X}_j^{n,1} - K_{n+1/2} \mathbf{Y}_j^{n,1}, \quad (\text{C.3})$$

$$\boldsymbol{\kappa}_j^{n,2} = S_{n+1} \mathbf{X}_j^{n,2} - K_{n+1/2} \mathbf{Y}_j^{n,2}, \quad (\text{C.4})$$

$$\boldsymbol{\ell}_j^{n,1} = K_n \mathbf{X}_j^{n,1} + S_{n+1/2} \mathbf{Y}_j^{n,1}, \quad (\text{C.5})$$

$$\boldsymbol{\ell}_j^{n,2} = K_{n+1} \mathbf{X}_j^{n,2} + S_{n+1/2} \mathbf{Y}_j^{n,2}. \quad (\text{C.6})$$

They are consistent approximations of the time derivatives  $\dot{\boldsymbol{\mu}}(t_n)$  and  $\dot{\boldsymbol{\nu}}(t_n)$ , respectively. The scheme is therefore a consistent approximation of the continuous adjoint system.

## Appendix D. Computing the gradient of the discrete objective function

Given a solution that satisfies the saddle point conditions of (41) and (42), the gradient of  $\mathcal{L}_h(\boldsymbol{\alpha})$  satisfies

$$\frac{d\mathcal{L}_h}{d\alpha_r} = \frac{\partial \mathcal{J}_{1h}}{\partial \alpha_r}(\mathbf{u}, \mathbf{v}) + \frac{\partial \mathcal{J}_{2h}}{\partial \alpha_r}(\mathbf{U}, \mathbf{V}), \quad r = 1, 2, \dots, D.$$

The gradient of  $\mathcal{L}_h$  with respect to  $\boldsymbol{\alpha}$  only gets a contribution from the terms in  $T_j^q$  that involve the matrices  $K$  and  $S$ . Let  $S'_n = \partial S / \partial \alpha_r(t_n)$  and  $K'_n = \partial K / \partial \alpha_r(t_n)$ . We have,

$$\begin{aligned} \frac{\partial T_j^1}{\partial \alpha_r} &= -\frac{h}{2} \sum_{n=0}^{M-1} \left\langle S'_n \mathbf{U}_j^{n,1} - K'_n \mathbf{V}_j^{n,1} + S'_{n+1} \mathbf{U}_j^{n,2} - K'_{n+1} \mathbf{V}_j^{n,2}, \boldsymbol{\mu}_j^{n+1} \right\rangle_2, \\ \frac{\partial T_j^2}{\partial \alpha_r} &= -\frac{h}{2} \sum_{n=0}^{M-1} \left\langle K'_{n+1/2} (\mathbf{U}_j^{n,1} + \mathbf{U}_j^{n,2}) + S'_{n+1/2} (\mathbf{V}_j^{n,1} + \mathbf{V}_j^{n,2}), \boldsymbol{\nu}_j^{n+1} \right\rangle_2, \\ \frac{\partial T_j^3}{\partial \alpha_r} &= 0, \\ \frac{\partial T_j^4}{\partial \alpha_r} &= -\frac{h}{2} \sum_{n=0}^{M-1} \left\langle S'_n \mathbf{U}_j^{n,1} - K'_n \mathbf{V}_j^{n,1} + S'_{n+1} \mathbf{U}_j^{n,2} - K'_{n+1} \mathbf{V}_j^{n,2}, \mathbf{M}_j^{n,2} \right\rangle_2, \\ \frac{\partial T_j^5}{\partial \alpha_r} &= -\frac{h}{2} \sum_{n=0}^{M-1} \left\langle K'_{n+1/2} \mathbf{U}_j^{n,1} + S'_{n+1/2} \mathbf{V}_j^{n,1}, \mathbf{N}_j^{n,1} \right\rangle_2, \\ \frac{\partial T_j^6}{\partial \alpha_r} &= -\frac{h}{2} \sum_{n=0}^{M-1} \left\langle K'_{n+1/2} \mathbf{U}_j^{n,1} + S'_{n+1/2} \mathbf{V}_j^{n,1}, \mathbf{N}_j^{n,2} \right\rangle_2. \end{aligned}$$

We note that

$$\frac{\partial(T_j^5 + T_j^6)}{\partial \alpha_r} = -\frac{h}{2} \sum_{n=0}^{M-1} \left\langle K'_{n+1/2} \mathbf{U}_j^{n,1} + S'_{n+1/2} \mathbf{V}_j^{n,1}, \mathbf{N}_j^{n,1} + \mathbf{N}_j^{n,2} \right\rangle_2.$$

Let  $\mathbf{X}_j^n$  and  $\mathbf{Y}_j^{n,i}$  be defined by (B.11)-(B.13). We have,

$$\begin{aligned} \frac{\partial T_j^4}{\partial \alpha_r} &= -\frac{h}{2} \sum_{n=0}^{M-1} \left\langle S'_n \mathbf{U}_j^{n,1} - K'_n \mathbf{V}_j^{n,1} + S'_{n+1} \mathbf{U}_j^{n,2} - K'_{n+1} \mathbf{V}_j^{n,2}, \mathbf{X}_j^n - \boldsymbol{\mu}_j^{n+1} \right\rangle_2, \\ \frac{\partial(T_j^5 + T_j^6)}{\partial \alpha_r} &= -\frac{h}{2} \sum_{n=0}^{M-1} \left\langle K'_{n+1/2} \mathbf{U}_j^{n,1} + S'_{n+1/2} \mathbf{V}_j^{n,1}, \mathbf{Y}_j^{n,1} - \boldsymbol{\nu}_j^{n+1} \right\rangle_2. \end{aligned}$$

Thus,

$$\frac{\partial(T_j^1 + T_j^4)}{\partial \alpha_r} = -\frac{h}{2} \sum_{n=0}^{M-1} \left\langle S'_n \mathbf{U}_j^{n,1} - K'_n \mathbf{V}_j^{n,1} + S'_{n+1} \mathbf{U}_j^{n,2} - K'_{n+1} \mathbf{V}_j^{n,2}, \mathbf{X}_j^n \right\rangle_2.$$

Furthermore, from the relation (B.13),

$$\begin{aligned} \frac{\partial(T_j^2 + T_j^5 + T_j^6)}{\partial\alpha_r} &= -\frac{\hbar}{2} \sum_{n=0}^{M-1} \left\langle K'_{n+1/2} \mathbf{U}_j^{n,1} + S'_{n+1/2} \mathbf{V}_j^{n,1}, \mathbf{Y}_j^{n,1} \right\rangle_2 \\ &\quad - \frac{\hbar}{2} \sum_{n=0}^{M-1} \left\langle K'_{n+1/2} \mathbf{U}_j^{n,2} + S'_{n+1/2} \mathbf{V}_j^{n,2}, \mathbf{Y}_j^{n,2} \right\rangle_2, \end{aligned}$$

We can further simplify the expressions by recognizing that  $\mathbf{V}^{n,1} = \mathbf{V}^{n,2}$ . By collecting the terms,

$$\begin{aligned} \frac{\partial\mathcal{L}_h}{\partial\alpha_r} &= \frac{\hbar}{2} \sum_{j=0}^{E-1} \sum_{n=0}^{M-1} \left( \left\langle S'_n \mathbf{U}_j^{n,1} + S'_{n+1} \mathbf{U}_j^{n,2} - (K'_n + K'_{n+1}) \mathbf{V}_j^{n,1}, \mathbf{X}_j^n \right\rangle_2 \right. \\ &\quad \left. + \left\langle K'_{n+1/2} \mathbf{U}_j^{n,1} + S'_{n+1/2} \mathbf{V}_j^{n,1}, \mathbf{Y}_j^{n,1} \right\rangle_2 \right. \\ &\quad \left. + \left\langle K'_{n+1/2} \mathbf{U}_j^{n,2} + S'_{n+1/2} \mathbf{V}_j^{n,1}, \mathbf{Y}_j^{n,2} \right\rangle_2 \right). \end{aligned}$$

This completes the proof of the lemma.

## References

- [1] Martín Abadi, Paul Barham, Jianmin Chen, Zhifeng Chen, Andy Davis, Jeffrey Dean, Matthieu Devin, Sanjay Ghemawat, Geoffrey Irving, Michael Isard, et al. Tensorflow: A system for large-scale machine learning. In *12th USENIX Symposium on Operating Systems Design and Implementation (OSDI 16)*, pages 265–283, 2016.
- [2] J. Bezanson, A. Edelman, S. Karpinski, and V. B. Shah. Julia: A fresh approach to numerical computing. *SIAM Review*, 59(1):65–89, 2017.
- [3] A. Borzì, G. Ciarmella, and M. Sprengel. *Formulation and Numerical Solution of Quantum Control Problems*. Computational science and engineering. SIAM, 2017.
- [4] T. Caneva, T. Calarco, and S. Montangero. Chopped random-basis quantum optimization. *Physical Review A*, 84(2), Aug 2011.
- [5] P. de Fouquieres, S.G. Schirmer, S.J. Glaser, and Ilya Kuprov. Second order gradient ascent pulse engineering. *Journal of Magnetic Resonance*, 212(2):412–417, Oct 2011.
- [6] L. Emsley and G. Bodenhausen. Gaussian pulse cascades: New analytical functions for rectangular selective inversion and in-phase excitation in NMR. *Chem. Phys.*, 165(6):469–476, 1989.
- [7] B. Ewing, S. J. Glaser, and G. P. Drobny. Development and optimization of shaped NMR pulses for the study of coupled spin systems. *Chem. Phys.*, 147:121–129, 1990.

- [8] G. H. Golub and C. F. Van Loan. *Matrix Computations*. Johns Hopkins University Press, 1996.
- [9] William W. Hager. Runge-Kutta methods in optimal control and the transformed adjoint system. *Numerische Mathematik*, 87(2):247–282, Dec 2000.
- [10] E. Hairer, C. Lubich, and G. Wanner. *Geometric Numerical Integration*. Number 31 in Springer series in computational mathematics. Springer-Verlag, Heidelberg, 2nd edition, 2006.
- [11] J.R. Johansson, P.D. Nation, and Franco Nori. Qutip 2: A python framework for the dynamics of open quantum systems. *Computer Physics Communications*, 184(4):1234 – 1240, 2013.
- [12] N. Khaneja, T. Reiss, C. Kehlet, T. Schulte-Herbruggen, and S. Glaser. Optimal control of coupled spin dynamics: design of NMR pulse sequences by gradient ascent algorithms. *J. Magnetic Resonance*, 172:296–305, 2005.
- [13] N. Leung, M. Abdelhafez, Jens Koch, and D. Schuster. Speedup for quantum optimal control from automatic differentiation based on graphics processing units. *Phys. Rev. A*, 95:0432318, 2017.
- [14] Dennis Lucarelli. Quantum optimal control via gradient ascent in function space and the time-bandwidth quantum speed limit. *Physical Review A*, 97(6), Jun 2018.
- [15] S. Machnes, E. Assémat, D. Tannor, and F. K. Wilhelm. Tunable, flexible, and efficient optimization of control pulses for practical qubits. *Physical Review Letters*, 120(15), Apr 2018.
- [16] M. Nielsen and I. Chuang. *Quantum computation and quantum information*. Cambridge University Press, 2000.
- [17] J. Nocedal and S. J. Wright. *Numerical Optimization*. Springer, 2nd edition, 2006.
- [18] Sina Ober-Blöbaum. *Discrete mechanics and optimal control*. PhD thesis, University of Paderborn, 2008.
- [19] J. M. Sanz-Serna. Symplectic Runge–Kutta schemes for adjoint equations, automatic differentiation, optimal control, and more. *SIAM Review*, 58(1):3–33, 2016.
- [20] Yunong Shi, Nelson Leung, Pranav Gokhale, Zane Rossi, David I. Schuster, Henry Hoffmann, and Frederic T. Chong. Optimized compilation of aggregated instructions for realistic quantum computers. *Proceedings of the Twenty-Fourth International Conference on Architectural Support for Programming Languages and Operating Systems - ASPLOS '19*, 2019.

- [21] A. Wächter and L. T. Biegler. On the implementation of an interior-point filter line-search algorithm for large-scale nonlinear programming. *Mathematical Programming*, 106(1):25–57, Mar 2006.
- [22] D. B. Zax, G. Goelman, and S. Vega. Amplitude-modulated composite pulses. *J. Magn. Reson.*, 80(2):375–382, 1988.